

# Dynamical modeling and lifetime analysis of geostationary transfer orbits



Yue Wang\*, Pini Gurfil

Distributed Space Systems Lab, Faculty of Aerospace Engineering, Technion–Israel Institute of Technology, Haifa 32000, Israel

## ARTICLE INFO

### Article history:

Received 20 September 2015

Received in revised form

13 May 2016

Accepted 30 June 2016

Available online 1 July 2016

### Keywords:

Geostationary transfer orbits

Semi-analytical orbital model

Orbital lifetime

Earth oblateness

Luni-solar perturbations

Atmospheric drag

## ABSTRACT

The dynamics and lifetime reduction of geostationary transfer orbits (GTOs) are of great importance to space debris mitigation. The orbital dynamics, subjected to a complex interplay of multiple perturbations, are complicated and sensitive to the initial conditions and model parameters. In this paper, a simple but effective non-singular orbital dynamics model in terms of Milankovitch elements is derived. The orbital dynamics, which include the Earth oblateness, luni-solar perturbations, and atmospheric drag, are averaged over the orbital motion of the GTO object, or, as needed, also over the orbital motions of the Moon and Sun, to eliminate the short-period terms. After the averaging process, the effect of the atmospheric drag assumes a simple analytical form. The averaged orbital model is verified through a numerical simulation compared with commercial orbit propagators. GTO lifetime reduction by using the luni-solar perturbations is studied. It is shown that the long-period luni-solar perturbation is induced by the precession of the GTO orbital plane and apsidal line, whereas the short-period perturbation is induced by the periodic luni-solar orbital motions. The long- and short-period perturbations are isolated and studied separately, and their global distribution with respect to the orbital geometry is given. The desired initial orbital geometry with a short orbital lifetime is found and verified by a numerical simulation.

© 2016 IAA. Published by Elsevier Ltd. All rights reserved.

## 1. Introduction

Geostationary transfer orbits (GTOs) have been broadly used to transfer satellites from circular low Earth orbits (LEOs) to geostationary orbits (GEOs). GTOs are highly eccentric orbits, characterized by a low perigee, normally at an altitude of 180–650 km, and a high apogee, near the geostationary altitude. After the payload is boosted into a GTO from a LEO, the spent upper stage is usually left uncontrolled in the GTO to become space debris. The upper stages, which are large objects and have large relative velocities, are a potential source for collisions and future debris. The space debris in GTOs have become a threat to satellites both in GEOs and LEOs, which are the two most important and populated orbital regions [1]. In this aspect, knowledge of the GTO dynamics under natural perturbations is needed for predicting the distribution, decay, and lifetime of the space debris. More importantly, a global picture of the dynamics will enable us to determine the optimal launch window with the minimum lifetime for spent upper stages, and to design the deorbit maneuvers.

Many have investigated the dynamical evolution, decay, and lifetime of GTOs, including King-Hele [2], Janin [3], Siebold and Reynolds [4], Takano et al. [5], Sharma et al. [6], Da Costa et al. [7], Morand et al. [8], Lamy et al. [9], Bonaventure et al. [10], and David and Braun [11]. King-Hele [2] developed an approximate analytical method for the lifetime prediction of highly eccentric transfer orbits. Janin [3] showed that the atmospheric drag at perigee may considerably change the orbital evolution of GTOs, and may render the lifetime prediction totally uncertain. Siebold and Reynolds [4] presented a model for reducing the orbital lifetime of GTOs with the help of the luni-solar perturbations. Takano et al. [5] also discussed the GTO orbital lifetime reduction by the luni-solar perturbations. Sharma et al. [6] investigated the basic physics of the luni-solar perturbations on GTOs and their interaction with the atmospheric drag, with special attention paid to the influence of the launch time on the orbital lifetime. Based on a semi-analytical solution of the Gauss equations, Da Costa et al. [7] have developed a long-term orbit propagator to integrate the natural decay of upper stages into the design process of European launchers. Morand et al. [8] and Lamy et al. [9] have studied the dynamical properties of GTOs over long time scales, especially the orbital lifetime estimation, by using numerical methods. Sharma et al. [6], Da Costa et al. [7], Morand et al. [8], and Lamy et al. [9] have all shown that the launch date and the local time of the initial perigee

\* Corresponding author.

E-mail addresses: [ywang.buaa@gmail.com](mailto:ywang.buaa@gmail.com) (Y. Wang), [pgurfil@technion.ac.il](mailto:pgurfil@technion.ac.il) (P. Gurfil).

have a strong impact on the orbital lifetime and even small changes in the launch time can result in large changes in the orbital lifetime. This strong impact and sensitivity are attributed to the solar third-body perturbation and the resonance between the solar orbital motion and the rotation of the apsidal line caused by Earth oblateness. Bonaventure et al. [10] have studied the de-orbiting maneuvers of the SPIRALE GTO satellites. David and Braun [11] investigated the influence of different methods for the solar activity forecasts on the residual lifetime of upper stages in GTOs.

Besides GTOs, there are other kinds of highly eccentric orbits, which are used for penetrating into the interplanetary space at a relative low energy, such as NASA's S-3 ( $e=0.867$ ), Eccentric Geophysical Observatories (EGO) ( $e=0.893$ ), Interplanetary Monitoring Platforms (IMP) ( $e=0.95$ ), and the European scientific satellite HEOS-1 ( $e=0.94$ ); or for communications in high latitudes, such as the Russian Molniya orbits ( $e=0.74$ ). These highly eccentric orbits, more eccentric than a GTO, are perturbed by the Moon and Sun more strongly, and are more unstable. The luni-solar perturbations induce an oscillation and bring the satellite back to Earth sooner or later. Many works have studied the dynamics and lifetime of these highly eccentric orbits to determine the launch window, see Upton et al. [12], Shute [13], Paddack and Shute [14], Shute and Chiville [15,16], Cook and Scott [17], and Janin and Roth [18]. As opposed to the case of space debris in GTOs, these works are aimed at guaranteeing a long enough orbital lifetime to meet mission requirements.

The studies on GTOs and highly eccentric orbits have revealed important characteristics of the dynamics. With a high eccentricity ( $e > 0.7$ ), the orbit has a low perigee and a high apogee, and then the orbital dynamics are subjected to a complex interplay of multiple perturbations, including Earth oblateness, luni-solar perturbations, and atmospheric drag.

The atmospheric drag takes effect near the perigee, reduces the semi-major axis, eccentricity, and apogee height, and finally ends the orbit when the perigee height is low enough. However, the orbital decay caused by the atmospheric drag alone takes a long time. The effect of atmospheric drag, which is predominant at altitudes lower than 300 km, strongly depends on the atmospheric density. Then, the fluctuation of the atmospheric density with the solar activity and the local time has a strong impact on the lifetime of GTOs [8,11]. The uncertainty of the atmospheric drag, induced by uncertainties of the atmospheric density and the cross-sectional area, renders the lifetime prediction of GTOs highly uncertain.

With the luni-solar perturbations affecting the orbit near apogee, the semi-major axis is kept nearly constant and the eccentricity has an oscillation with the perigee height decreasing or increasing, as shown by Janin [3], Siebold and Reynolds [4], Da Costa et al. [7], and Morand et al. [8]. The eccentricity oscillation is a superposition of a long-period oscillation with a period of several years and two relatively short-period oscillations, which are associated with the orbital motions of the Moon and Sun, with periods of about 14 days and 180 days, respectively, i.e., half the orbital periods of the perturbing bodies, as shown by Shute [13], Paddack and Shute [14], Shute and Chiville [15,16], Cook and Scott [17], and Fischer [19]. The initial phase of the long-period oscillation is determined by the initial relative geometry of the luni-solar orbital planes with respect to the orbit's apsidal line, as shown by Kozai [20] and Shute [13], while the initial phases of the 14-day and 180-day oscillations are determined by initial relative positions (azimuths) of the Moon and Sun with respect to the orbit's apsidal line, respectively, as shown by Shute [13], and Shute and Chiville [15].

The orbital lifetime is determined by both the perigee height change by the luni-solar perturbations and the decaying effect of the atmospheric drag. Through the eccentricity oscillation, the

luni-solar perturbations can lower or raise the initial perigee height remarkably, i.e., can reduce or enhance the orbital lifetime. The amplitudes of the 14-day and 180-day perigee height oscillations are 15 km and 100 km for the S-3 satellite, and 25–35 km and 100–200 km for the EGO satellite, as shown by Shute [13]. The resultant curve of the perigee height is a superposition of the long-period oscillation and two short-period oscillations, and the trend of its variation is determined by the initial phases and amplitudes of these oscillations. Siebold and Reynolds [4], Takano et al. [5], and Sharma et al. [6] have shown that by choosing a proper launch window, which determines the initial orbital geometry and then determines the initial phases of oscillations, the luni-solar perturbations can be used to lower the initial perigee height and cause the space debris to decay quickly. Conversely, Upton et al. [12], Shute [13], Paddack and Shute [14], Shute and Chiville [15,16], Cook and Scott [17] have tried to find the launch window for the desired initial phases of oscillations, so that the initial perigee is raised by the luni-solar perturbations after launch and a long lifetime can be achieved.

With the perturbation of Earth oblateness only, the orbital plane and apsidal line will precess with the orbital shape nearly unchanged. Therefore, Earth oblateness alone is not directly responsible for the natural orbit decay. However, Earth oblateness has a significant indirect effect on the orbital evolution and lifetime. The precession of the orbital plane and apsidal line will change the relative geometry of the Moon and Sun with respect to the orbit apsides, which will in turn change the luni-solar effect on the eccentricity, as shown by Shute [13], Cook and Scott [17], Janin [3], Siebold and Reynolds [4], Sharma et al. [6], Da Costa et al. [7], and Morand et al. [8].

In particular, a 1:1 resonance between the solar orbital motion and the apsidal line precession caused by Earth oblateness can exist when the semi-major axis and eccentricity are reduced by the atmospheric drag to the resonance condition. This solar apsidal resonance keeps a nearly constant Sun azimuth with respect to the orbit apsides, and the 180-day eccentricity oscillation becomes a monotonically increasing or decreasing for a relatively long duration. Then, the solar perturbation will lower or raise the perigee height continuously, as shown by Sharma et al. [6], Da Costa et al. [7], Morand et al. [8], Lamy et al. [9], Bonaventure et al. [10], and Le Fèvre et al. [21]. The continuous lowering or raising of the perigee height during the solar apsidal resonance can totally change the orbital evolution and lifetime. Moreover, the solar apsidal resonance is highly sensitive to the initial conditions, computational accuracy and the model parameters of the perturbations, and then it can be neither predicted nor managed, as shown by Da Costa et al. [7], Morand et al. [8], Lamy et al. [9], and Bonaventure et al. [10]. This is exactly the mechanism behind the phenomenon wherein small launch time changes can result in large orbital lifetime changes, as reported by Sharma et al. [8], Da Costa et al. [7], Morand et al. [8] and Le Fèvre et al. [21].

As stated above, the orbital evolution and lifetime of the highly eccentric orbits are determined by the complex interplay between the Earth oblateness, luni-solar perturbations and atmospheric drag. The dynamical evolution is complicated and sensitive to initial conditions and model parameters. Although previous works, most of which used numerical methods, have revealed many important characteristics, more rigorous insights and a global analysis of the dynamics are still required.

In the present paper, we will investigate the orbital dynamics and lifetime reduction of GTOs based on a simple, but effective, averaged orbital dynamics model formulated in terms of Milankovitch elements. The Milankovitch elements use two vectorial integrals, the angular momentum vector  $\mathbf{H}$  and the Laplace vector  $\mathbf{b}$ , to describe the orientation, shape, and size of the osculating Keplerian orbit [22]. The elements, which are free of singularities

associated with the zero eccentricity and vanishing line of nodes, have recently been used in the investigation of long-term dynamics of high area-to-mass ratio objects in high-Earth orbits [23,24]. The orbital variational equations formulated in terms of Milankovitch elements are suitable for the orbital dynamical analysis due to their concise vectorial form and explicit relation with the underlying physics. By averaging the orbital dynamics, the short-period perturbation terms can be eliminated and equations of motion that capture the secular system evolution can be derived. By using this approach, we can capture the dynamical features more clearly.

In this study, the orbital model is derived by using the Gauss equations. Then, the orbital model is averaged over the orbital motion on the GTO, as well as the orbital motions of the Moon and Sun, to eliminate corresponding short-period terms. After the averaging process, the effect of the atmospheric drag assumes a simple analytical form. These averaged dynamical models are verified through a numerical simulation compared with the High Precision Orbit Propagator (HPOP) and Long-term Orbit Predictor (LOP) in the Systems Tool Kit (STK). Finally, GTO lifetime reduction by using the luni-solar perturbations is studied based on the averaged orbital model.

Compared to previous works, this study will provide a new singularity-free semi-analytical orbital model formulated in terms of Milankovitch elements, which accounts for the main effects of Earth oblateness, luni-solar perturbations, and atmospheric drag. This simplified semi-analytical model can provide a computationally efficient portrayal of the orbital evolution, and is useful for the orbit propagation in a time span of several years. Another contribution of this paper is a thorough study of the luni-solar perturbations and the application thereof to GTO lifetime reduction. The long- and short-period perturbations are isolated and analyzed separately; a direct relation between the perturbation effects and the orbital geometry is achieved; and finally, the initial orbital geometry providing the minimum orbital lifetime is found.

## 2. Milankovitch orbital elements

The Milankovitch elements contain two vectorial integrals: the specific angular momentum vector  $\mathbf{H}$ , normal to the instantaneous orbital plane, and the Laplace vector  $\mathbf{b} = \mu \mathbf{e}$ , pointing towards the instantaneous perigee, where  $\mu$  is the gravitational constant of Earth and  $\mathbf{e}$  is the eccentricity vector. The magnitude of  $\mathbf{H}$  is  $\sqrt{\mu a(1 - e^2)}$ , where  $a$  is the semi-major axis. The angular momentum and eccentricity vectors satisfy the identity  $\mathbf{H} \cdot \mathbf{e} = 0$ , and a sixth scalar representing the motion in orbit is needed to constitute a complete set of orbital elements. The vectors  $\mathbf{H}$  and  $\mathbf{e}$  can be written in terms of the position  $\mathbf{r}$  and velocity  $\mathbf{v}$  as

$$\mathbf{H} = \mathbf{r} \times \mathbf{v}, \quad (1)$$

$$\mathbf{e} = \frac{1}{\mu} \mathbf{v} \times \mathbf{r} - \frac{\mathbf{r}}{r}, \quad (2)$$

where

$$\mathbf{r}^\times = \begin{bmatrix} 0 & -r^z & r^y \\ r^z & 0 & -r^x \\ -r^y & r^x & 0 \end{bmatrix}, \quad \mathbf{v}^\times = \begin{bmatrix} 0 & -v^z & v^y \\ v^z & 0 & -v^x \\ -v^y & v^x & 0 \end{bmatrix}, \quad (3)$$

i.e.,  $\mathbf{r}^\times \mathbf{v} = \mathbf{r} \times \mathbf{v}$  and  $\mathbf{v}^\times \mathbf{r} = \mathbf{v} \times (\mathbf{r} \times \mathbf{v})$ .

The mean longitude  $l$ , which can be used as the sixth scalar, is defined as

$$l = \Omega + \omega + M, \quad (4)$$

where  $\Omega$  is the right ascension of the ascending node (RAAN),  $\omega$  is the argument of perigee, and  $M$  is the mean anomaly.

The averaged dynamics in terms of Milankovitch elements under the perturbations of the Earth oblateness and luni-solar gravity were obtained by using the Lagrange planetary equations [23]. Here, we need to incorporate the perturbation of atmospheric drag into the averaged orbital dynamics; therefore, the Gauss equations in terms of Milankovitch elements and the averaging process over the mean anomaly are needed.

The Gauss equations for the Milankovitch elements  $\mathbf{H}$  and  $\mathbf{e}$  are given by [25]

$$\dot{\mathbf{H}} = \mathbf{r}^\times \mathbf{a}_p, \quad (5)$$

$$\dot{\mathbf{e}} = \frac{1}{\mu} (\mathbf{v}^\times \mathbf{r}^\times - \mathbf{H}^\times) \mathbf{a}_p, \quad (6)$$

where  $\mathbf{a}_p$  is the perturbing acceleration.

By averaging the Gauss equations over the mean anomaly, the variational equations of  $\mathbf{H}$  and  $\mathbf{e}$  without the short-period terms associated with the orbital motion on the GTO can be obtained as

$$\dot{\bar{\mathbf{H}}} = \frac{1}{2\pi} \int_0^{2\pi} \dot{\mathbf{H}} dM = \frac{1}{2\pi} \int_0^{2\pi} \mathbf{r}^\times \mathbf{a}_p dM, \quad (7)$$

$$\dot{\bar{\mathbf{e}}} = \frac{1}{2\pi} \int_0^{2\pi} \dot{\mathbf{e}} dM = \frac{1}{2\pi} \int_0^{2\pi} \frac{1}{\mu} (\mathbf{v}^\times \mathbf{r}^\times - \mathbf{H}^\times) \mathbf{a}_p dM, \quad (8)$$

where  $\bar{(\cdot)}$  denotes the averaged value over one orbit.

The relations between the Milankovitch elements  $\{\mathbf{H}, \mathbf{e}\}$  and the classical orbital elements  $\{a, e, i, \Omega, \omega\}$ , which are defined with respect to a standard Earth-centered inertial reference frame  $S = \{\hat{\mathbf{x}}, \hat{\mathbf{y}}, \hat{\mathbf{z}}\}$ , are given by

$$e = |\mathbf{e}|, \quad a = \frac{H^2}{\mu(1 - e^2)}, \quad \cos i = \hat{\mathbf{z}} \cdot \hat{\mathbf{H}}, \quad (9)$$

$$\cos \Omega = -\frac{\hat{\mathbf{y}} \cdot \hat{\mathbf{H}}}{|\hat{\mathbf{z}} \times \hat{\mathbf{H}}|}, \quad \sin \Omega = \frac{\hat{\mathbf{x}} \cdot \hat{\mathbf{H}}}{|\hat{\mathbf{z}} \times \hat{\mathbf{H}}|}, \quad (10)$$

$$\cos \omega = \frac{\mathbf{e} \cdot (\hat{\mathbf{z}} \times \hat{\mathbf{H}})}{e |\hat{\mathbf{z}} \times \hat{\mathbf{H}}|}, \quad \sin \omega = \frac{\mathbf{e} \cdot (\hat{\mathbf{H}} \times \hat{\mathbf{z}} \times \hat{\mathbf{H}})}{e |\hat{\mathbf{H}} \times \hat{\mathbf{z}} \times \hat{\mathbf{H}}|}. \quad (11)$$

## 3. Averaged orbital dynamics

By using previous results [23], three different averaged orbital models are obtained: a singly-averaged model; a doubly-averaged model with the averaging performed over the orbital motion on the GTO and the orbital motion of the Moon; and a triply-averaged model with the averaging performed over the orbital motion on the GTO and the orbital motions of the Moon and Sun.

### 3.1. Averaged dynamics with $J_2$ and luni-solar perturbations

The singly- and doubly-averaged orbital dynamics under  $J_2$  and luni-solar perturbations have been derived in terms of  $\mathbf{h}$  and  $\mathbf{e}$ , where the angular momentum vector  $\mathbf{H}$  is scaled as  $\mathbf{h} = \mathbf{H} / \sqrt{\mu a}$  since the semi-major axis  $a$  has no secular change after averaging [23].

The singly-averaged variational equation of  $\mathbf{h}$ , in which the

averaging process is performed over the mean anomaly of the GTO, is given by [23]

$$\begin{aligned}\dot{\mathbf{h}} = \dot{\mathbf{h}}_{J_2} + \dot{\mathbf{h}}_S + \dot{\mathbf{h}}_M = & -\frac{3\bar{n}J_2R_E^2}{2a^2\bar{h}^5}(\hat{\mathbf{p}}\cdot\bar{\mathbf{h}})\hat{\mathbf{p}}^\times\bar{\mathbf{h}} \\ & + \frac{3\mu_S}{2\bar{n}d_S^3}\left[5(\hat{\mathbf{d}}_S\cdot\bar{\mathbf{e}})\bar{\mathbf{e}}^\times\hat{\mathbf{d}}_S - (\hat{\mathbf{d}}_S\cdot\bar{\mathbf{h}})\bar{\mathbf{h}}^\times\hat{\mathbf{d}}_S\right] \\ & + \frac{3\mu_M}{2\bar{n}d_M^3}\left[5(\hat{\mathbf{d}}_M\cdot\bar{\mathbf{e}})\bar{\mathbf{e}}^\times\hat{\mathbf{d}}_M - (\hat{\mathbf{d}}_M\cdot\bar{\mathbf{h}})\bar{\mathbf{h}}^\times\hat{\mathbf{d}}_M\right],\end{aligned}\quad (12)$$

where  $n = \sqrt{\mu/a^3}$  is the mean motion,  $R_E$  is the mean equatorial radius of the Earth,  $\hat{\mathbf{p}}$  is the spin axis of the Earth,  $\mu_S$  and  $\mu_M$  are the gravitational constants of the Sun and Moon, respectively, and  $\mathbf{d}_S$  and  $\mathbf{d}_M$  are the position vectors of the Sun and Moon relative to Earth, respectively.

In Eq. (12), the effect of  $J_2$  is taken into account. As for the luni-solar perturbations, the Legendre expansion of the disturbing function is retained up to the second order by using the Hill approximation. This approximation is valid only when the distance between the satellite and Earth is small compared to the distance of the third body from Earth. Cook and Scott [17] showed that when the semi-major axis is smaller than 10 Earth radii, the Hill approximation can capture the lunar perturbation quite well. Therefore, the Hill approximation is sufficient for GTOs. The validity of these approximations will be verified by a numerical simulation in Section 4.

Due to the atmospheric drag, the semi-major axis of a GTO will be reduced; therefore, the averaged equation of  $\mathbf{h}$  given by Eq. (12) needs to be rewritten in terms of the angular momentum vector  $\mathbf{H}$ . Taking the product of both sides of Eq. (12) with  $\sqrt{\mu a}$  yields the singly-averaged variational equation of  $\mathbf{H}$ ,

$$\begin{aligned}\dot{\mathbf{H}} = \dot{\mathbf{H}}_{J_2} + \dot{\mathbf{H}}_S + \dot{\mathbf{H}}_M \\ = & -\frac{3\mu J_2 R_E^2}{2a^3\bar{h}^5}(\hat{\mathbf{p}}\cdot\bar{\mathbf{h}})\hat{\mathbf{p}}^\times\bar{\mathbf{h}} \\ & + \frac{3\bar{a}^2\mu_S}{2d_S^3}\left[5(\hat{\mathbf{d}}_S\cdot\bar{\mathbf{e}})\bar{\mathbf{e}}^\times\hat{\mathbf{d}}_S - (\hat{\mathbf{d}}_S\cdot\bar{\mathbf{h}})\bar{\mathbf{h}}^\times\hat{\mathbf{d}}_S\right] \\ & + \frac{3\bar{a}^2\mu_M}{2d_M^3}\left[5(\hat{\mathbf{d}}_M\cdot\bar{\mathbf{e}})\bar{\mathbf{e}}^\times\hat{\mathbf{d}}_M - (\hat{\mathbf{d}}_M\cdot\bar{\mathbf{h}})\bar{\mathbf{h}}^\times\hat{\mathbf{d}}_M\right].\end{aligned}\quad (13)$$

The singly-averaged variational equation of  $\mathbf{e}$  under  $J_2$  and luni-solar perturbations is given by [23]

$$\begin{aligned}\dot{\mathbf{e}} = \dot{\mathbf{e}}_{J_2} + \dot{\mathbf{e}}_S + \dot{\mathbf{e}}_M \\ = & -\frac{3\bar{n}J_2R_E^2}{4\bar{a}^2\bar{h}^5}\left\{\left[1 - \frac{5}{\bar{h}^2}(\hat{\mathbf{p}}\cdot\bar{\mathbf{h}})^2\right]\bar{\mathbf{h}}^\times + 2(\hat{\mathbf{p}}\cdot\bar{\mathbf{h}})\hat{\mathbf{p}}^\times\right\}\bar{\mathbf{e}} \\ & + \frac{3\mu_S}{2\bar{n}d_S^3}\left[5(\hat{\mathbf{d}}_S\cdot\bar{\mathbf{e}})\bar{\mathbf{h}}^\times\hat{\mathbf{d}}_S - (\hat{\mathbf{d}}_S\cdot\bar{\mathbf{h}})\bar{\mathbf{e}}^\times\hat{\mathbf{d}}_S - 2\bar{\mathbf{h}}^\times\bar{\mathbf{e}}\right] \\ & + \frac{3\mu_M}{2\bar{n}d_M^3}\left[5(\hat{\mathbf{d}}_M\cdot\bar{\mathbf{e}})\bar{\mathbf{h}}^\times\hat{\mathbf{d}}_M - (\hat{\mathbf{d}}_M\cdot\bar{\mathbf{h}})\bar{\mathbf{e}}^\times\hat{\mathbf{d}}_M - 2\bar{\mathbf{h}}^\times\bar{\mathbf{e}}\right].\end{aligned}\quad (14)$$

If the singly-averaged variational Eqs. (13) and (14) are further averaged over the orbital motion of the Moon to eliminate the 14-day short-period terms, the doubly-averaged variational equations can be obtained as

$$\begin{aligned}\dot{\mathbf{H}} = \dot{\mathbf{H}}_{J_2} + \dot{\mathbf{H}}_S + \dot{\mathbf{H}}_M = & -\frac{3\mu J_2 R_E^2}{2\bar{a}^3\bar{h}^5}(\hat{\mathbf{p}}\cdot\bar{\mathbf{h}})\hat{\mathbf{p}}^\times\bar{\mathbf{h}} \\ & + \frac{3\bar{a}^2\mu_S}{2d_S^3}\left[5(\hat{\mathbf{d}}_S\cdot\bar{\mathbf{e}})\bar{\mathbf{e}}^\times\hat{\mathbf{d}}_S - (\hat{\mathbf{d}}_S\cdot\bar{\mathbf{h}})\bar{\mathbf{h}}^\times\hat{\mathbf{d}}_S\right] \\ & - \frac{3\bar{a}^2\mu_M}{4\bar{a}_M^3h_M^3}\left[5(\hat{\mathbf{H}}_M\cdot\bar{\mathbf{e}})\bar{\mathbf{e}}^\times\hat{\mathbf{H}}_M - (\hat{\mathbf{H}}_M\cdot\bar{\mathbf{h}})\bar{\mathbf{h}}^\times\hat{\mathbf{H}}_M\right],\end{aligned}\quad (15)$$

$$\begin{aligned}\dot{\mathbf{e}} = \dot{\mathbf{e}}_{J_2} + \dot{\mathbf{e}}_S + \dot{\mathbf{e}}_M \\ = & -\frac{3\bar{n}J_2R_E^2}{4\bar{a}^2\bar{h}^5}\left\{\left[1 - \frac{5}{\bar{h}^2}(\hat{\mathbf{p}}\cdot\bar{\mathbf{h}})^2\right]\bar{\mathbf{h}}^\times + 2(\hat{\mathbf{p}}\cdot\bar{\mathbf{h}})\hat{\mathbf{p}}^\times\right\}\bar{\mathbf{e}} \\ & + \frac{3\mu_S}{2\bar{n}d_S^3}\left[5(\hat{\mathbf{d}}_S\cdot\bar{\mathbf{e}})\bar{\mathbf{h}}^\times\hat{\mathbf{d}}_S - (\hat{\mathbf{d}}_S\cdot\bar{\mathbf{h}})\bar{\mathbf{e}}^\times\hat{\mathbf{d}}_S - 2\bar{\mathbf{h}}^\times\bar{\mathbf{e}}\right] \\ & - \frac{3\mu_M}{4\bar{n}a_M^3h_M^3}\left[5(\hat{\mathbf{H}}_M\cdot\bar{\mathbf{e}})\bar{\mathbf{h}}^\times\hat{\mathbf{H}}_M - (\hat{\mathbf{H}}_M\cdot\bar{\mathbf{h}})\bar{\mathbf{e}}^\times\hat{\mathbf{H}}_M - 2\bar{\mathbf{h}}^\times\bar{\mathbf{e}}\right],\end{aligned}\quad (16)$$

where  $h_M = \sqrt{1 - e_M^2}$ , and  $a_M$ ,  $e_M$  and  $\mathbf{H}_M$  are the semi-major axis, eccentricity, and angular momentum of the Moon's orbit, respectively.

If Eqs. (15) and (16) are further averaged over the orbital motion of the Sun to eliminate the 180-day short-period terms, then the triply-averaged variational equations can be obtained as

$$\begin{aligned}\dot{\mathbf{H}} = \dot{\mathbf{H}}_{J_2} + \dot{\mathbf{H}}_S + \dot{\mathbf{H}}_M = & -\frac{3\mu J_2 R_E^2}{2\bar{a}^3\bar{h}^5}(\hat{\mathbf{p}}\cdot\bar{\mathbf{h}})\hat{\mathbf{p}}^\times\bar{\mathbf{h}} \\ & - \frac{3\bar{a}^2\mu_S}{4\bar{a}_S^3h_S^3}\left[5(\hat{\mathbf{H}}_S\cdot\bar{\mathbf{e}})\bar{\mathbf{e}}^\times\hat{\mathbf{H}}_S - (\hat{\mathbf{H}}_S\cdot\bar{\mathbf{h}})\bar{\mathbf{h}}^\times\hat{\mathbf{H}}_S\right] \\ & - \frac{3\bar{a}^2\mu_M}{4\bar{a}_M^3h_M^3}\left[5(\hat{\mathbf{H}}_M\cdot\bar{\mathbf{e}})\bar{\mathbf{e}}^\times\hat{\mathbf{H}}_M - (\hat{\mathbf{H}}_M\cdot\bar{\mathbf{h}})\bar{\mathbf{h}}^\times\hat{\mathbf{H}}_M\right],\end{aligned}\quad (17)$$

$$\begin{aligned}\dot{\mathbf{e}} = \dot{\mathbf{e}}_{J_2} + \dot{\mathbf{e}}_S + \dot{\mathbf{e}}_M \\ = & -\frac{3\bar{n}J_2R_E^2}{4\bar{a}^2\bar{h}^5}\left\{\left[1 - \frac{5}{\bar{h}^2}(\hat{\mathbf{p}}\cdot\bar{\mathbf{h}})^2\right]\bar{\mathbf{h}}^\times + 2(\hat{\mathbf{p}}\cdot\bar{\mathbf{h}})\hat{\mathbf{p}}^\times\right\}\bar{\mathbf{e}} \\ & - \frac{3\mu_S}{4\bar{n}a_S^3h_S^3}\left[5(\hat{\mathbf{H}}_S\cdot\bar{\mathbf{e}})\bar{\mathbf{h}}^\times\hat{\mathbf{H}}_S - (\hat{\mathbf{H}}_S\cdot\bar{\mathbf{h}})\bar{\mathbf{e}}^\times\hat{\mathbf{H}}_S - 2\bar{\mathbf{h}}^\times\bar{\mathbf{e}}\right] \\ & - \frac{3\mu_M}{4\bar{n}a_M^3h_M^3}\left[5(\hat{\mathbf{H}}_M\cdot\bar{\mathbf{e}})\bar{\mathbf{h}}^\times\hat{\mathbf{H}}_M - (\hat{\mathbf{H}}_M\cdot\bar{\mathbf{h}})\bar{\mathbf{e}}^\times\hat{\mathbf{H}}_M - 2\bar{\mathbf{h}}^\times\bar{\mathbf{e}}\right],\end{aligned}\quad (18)$$

where  $h_S = \sqrt{1 - e_S^2}$ , and  $a_S$ ,  $e_S$  and  $\mathbf{H}_S$  are the semi-major axis, eccentricity, and angular momentum of the Sun's orbit, respectively.

### 3.2. Averaged dynamics with atmospheric drag

Based on the free molecular flow theory, the perturbing acceleration acting on a satellite of mass  $m$  due to the atmospheric drag expressed in an inertial frame is given by [26]

$$\mathbf{a}_{\text{drag}} = -\frac{1}{2}\rho\frac{SC_D}{m}|\mathbf{v} - \mathbf{v}_{\text{atm}}|(\mathbf{v} - \mathbf{v}_{\text{atm}}),\quad (19)$$

where  $\rho$  is the atmospheric density,  $S$  is the cross-sectional area of

the satellite perpendicular to the relative velocity  $\mathbf{v} - \mathbf{v}_{atm}$ ,  $C_D$  is the non-dimensional drag coefficient, and  $\mathbf{v}_{atm}$  is the atmospheric velocity. For a general satellite or rocket upper stage, the value of the drag coefficient  $C_D$  is suggested to be 2.2 [26].

As for the area-to-mass ratio (AMR)  $S/m$ , we have some parameters for the two typical upper stages of the European launcher Ariane 5<sup>1,2</sup>:

(a) EPS (Étage à Propergols Stockables-Storable Propellant Stage) with the Aestus engine used in Ariane 5 GS with a GTO payload mass of 6.64 tons, length = 3.4 m, diameter = 5.4 m, empty mass = 1.2 tons, the AMR is about 0.0153–0.0191 m<sup>2</sup>/kg;

(b) ESC-A (Étage Supérieur Cryotechnique de type A-Cryogenic Upper Stage A) with the HM-7B engine used in Ariane 5 ECA with a GTO payload mass of 10 tons, length = 4.711 m, diameter = 5.4 m, empty mass = 4.54 tons, the AMR is about 0.0050–0.0056 m<sup>2</sup>/kg.

These two typical upper stages, EPS and ESC-A, used for single and dual launches of 5-ton GEO satellites into a GTO, respectively, are representative of present and past GEO launchers. Also, according to the RAE Tables of Artificial Satellites,<sup>3</sup> the considered range of AMR is set to be 0.005–0.02 m<sup>2</sup>/kg, which covers almost all the spent upper stages in GTOs.

To achieve an analytical form for the perturbation of atmospheric drag, an approximation that has been widely used in semi-analytical orbital theories is adopted, that is, the atmospheric velocity  $\mathbf{v}_{atm}$  is neglected [26]. Then, the atmospheric perturbing acceleration (19) can be simplified into

$$\mathbf{a}_{drag} = -\frac{1}{2}\rho B \mathbf{v} \mathbf{v}, \quad (20)$$

where  $B = SC_D/m$  is the ballistic coefficient.

As for the atmospheric density  $\rho$ , it is assumed that the density depends solely on the distance  $r$  from the Earth center, i.e., the atmosphere has a spherical symmetry, and the density varies exponentially with  $r$ . Thus,

$$\rho = \rho_{p0} \exp\left(-\frac{r - r_{p0}}{H_\rho}\right), \quad (21)$$

where  $\rho_{p0}$  and  $r_{p0}$  are the atmospheric density and the distance from Earth center at the initial perigee, respectively, and  $H_\rho$  is a constant scale height. This is a quite simple model of the atmospheric density, but as will be shown in Section 4, it is sufficient to capture the main effect of the atmospheric drag on the GTO. Note that this model does not take into account the solar activity, which may have a strong impact on the atmospheric density and on the evolution of GTOs [8,11].

By averaging, the effect of the atmospheric drag can be obtained in a simple analytical form. According to Eqs. (5), (6), and (20),

$$\dot{\mathbf{H}}_{Atm} = \mathbf{r}^\times \mathbf{a}_{drag} = -\frac{1}{2}\rho B \mathbf{v} \mathbf{r}^\times \mathbf{v} = -\frac{1}{2}\rho B \mathbf{v} \mathbf{H}, \quad (22)$$

$$\begin{aligned} \dot{\mathbf{e}}_{Atm} &= \frac{1}{\mu}(\mathbf{v}^\times \mathbf{r}^\times - \mathbf{H}^\times) \mathbf{a}_{drag} = \frac{1}{\mu} \left( -\frac{1}{2}\rho B \mathbf{v} \mathbf{v}^\times \mathbf{r}^\times \mathbf{v} + \frac{1}{2}\rho B \mathbf{v} \mathbf{H}^\times \mathbf{v} \right) \\ &= \frac{1}{\mu} \rho B \mathbf{v} \mathbf{H}^\times \mathbf{v}. \end{aligned} \quad (23)$$

By using Eqs. (7) and (8), the averaging process performed on Eqs. (22) and (23) over the mean anomaly of the GTO can be given as

$$\begin{aligned} \dot{\mathbf{H}}_{Atm} &= \frac{1}{2\pi} \int_0^{2\pi} \left( -\frac{1}{2}\rho B \mathbf{v} \mathbf{H} \right) dM = -\frac{1}{2} B \mathbf{H} \frac{1}{2\pi} \int_0^{2\pi} \rho v dM \\ &= -\frac{1}{2} B \mathbf{H} \bar{\rho} \bar{v}, \end{aligned} \quad (24)$$

$$\begin{aligned} \dot{\mathbf{e}}_{Atm} &= \frac{1}{2\pi} \int_0^{2\pi} \frac{1}{\mu} \rho B \mathbf{v} \mathbf{H}^\times \mathbf{v} dM = \frac{1}{\mu} B \mathbf{H}^\times \frac{1}{2\pi} \int_0^{2\pi} \rho v \mathbf{v} dM \\ &= \frac{1}{\mu} B \mathbf{H}^\times \bar{\rho} \bar{v} \mathbf{v}. \end{aligned} \quad (25)$$

To obtain the averaged values  $\bar{\rho} \mathbf{v}$  and  $\bar{\rho} \mathbf{v} \mathbf{v}$  in Eqs. (24) and (25), using the identities  $r_{p0} = a_0(1 - e_0)$  and  $r = a(1 - e \cos E)$ , we re-write the atmospheric density, Eq. (21), into

$$\rho = \rho_{p0} \exp\left[\frac{1}{H_\rho}(a_0 - a_0 e_0 - a) + \frac{1}{H_\rho} a e \cos E\right], \quad (26)$$

where  $E$  is the eccentric anomaly.

By using the relation

$$dM = \frac{r}{a} dE \quad (27)$$

and Eq. (26), the averaged value  $\bar{\rho} \mathbf{v}$  in Eq. (24) can be written as

$$\begin{aligned} \bar{\rho} \mathbf{v} &= \frac{1}{2\pi} \int_0^{2\pi} \rho v dM = \frac{1}{2\pi a} \rho_{p0} \exp\left(\frac{a_0 - a_0 e_0 - a}{H_\rho}\right) \\ &\quad \int_0^{2\pi} \exp\left(\frac{a e \cos E}{H_\rho}\right) v r dE. \end{aligned} \quad (28)$$

Since the velocity  $\mathbf{v}$  is given by

$$\mathbf{v} = \frac{\sqrt{\mu a}}{r} \left( -\sin E \hat{\mathbf{e}} + \sqrt{1 - e^2} \cos E \hat{\mathbf{e}}_1 \right), \quad (29)$$

where  $\hat{\mathbf{e}}_1 = \hat{\mathbf{H}} \times \hat{\mathbf{e}}$ , and

$$v = \frac{\sqrt{\mu a}}{r} \sqrt{1 - e^2 \cos^2 E}, \quad (30)$$

then the averaged value  $\bar{\rho} \mathbf{v}$  in Eq. (28) can be written as

$$\begin{aligned} \bar{\rho} \mathbf{v} &= \frac{1}{2\pi} \sqrt{\frac{\mu}{a}} \rho_{p0} \exp\left(\frac{a_0 - a_0 e_0 - a}{H_\rho}\right) \\ &\quad \int_0^{2\pi} \exp(z \cos E) \sqrt{1 - e^2 \cos^2 E} dE, \end{aligned} \quad (31)$$

where

$$z = \frac{a e}{H_\rho}. \quad (32)$$

According to King-Hele [26], substituting

$$\cos E = 1 - \frac{\lambda^2}{z}, \quad (33)$$

we have

$$dE = \sqrt{\frac{2}{z(1 - \lambda^2/2z)}} d\lambda. \quad (34)$$

Substituting Eqs. (33) and (34) into Eq. (31), and expanding the integrands into powers of  $\frac{\lambda^2}{z}$ , we have

<sup>1</sup> Ariane 5 Data Sheet. <http://www.spacelaunchreport.com/ariane5.html>

<sup>2</sup> [http://en.wikipedia.org/wiki/Ariane\\_5](http://en.wikipedia.org/wiki/Ariane_5)

<sup>3</sup> <http://www.satlist.nl/>



$$\begin{aligned}
\bar{\rho v} &= \frac{1}{\pi} \sqrt{\frac{\mu}{a}} \rho_{p0} \exp \left( \frac{a_0 - a_0 e_0 - a}{H_p} \right) \\
&\times \int_0^{\sqrt{2z}} \exp \left( (z - \lambda^2) \sqrt{1 - e^2} \sqrt{1 - \frac{e^2}{1 - e^2} \left( \frac{\lambda^4}{z^2} - 2 \frac{\lambda^2}{z} \right)} \right. \\
&\left. \sqrt{\frac{2}{z(1 - \lambda^2/2z)}} d\lambda = \frac{1}{\pi} \sqrt{\frac{\mu}{a}} \rho_{p0} \sqrt{1 - e^2} \sqrt{\frac{2}{z}} \right. \\
&\left. \exp \left( \frac{r_{p0} - r_p}{H_p} \right) \right. \\
&\times \int_0^{\sqrt{2z}} \exp(-\lambda^2) \left[ 1 + \frac{1 + 3e^2}{4(1 - e^2)} \frac{\lambda^2}{z} \right. \\
&\left. + \frac{3 - 14e^2 - 5e^4}{32(1 - e^2)^2} \frac{\lambda^4}{z^2} + O \left( \frac{\lambda^6}{z^3} \right) \right] d\lambda. \quad (35)
\end{aligned}$$

Here, the expansion is truncated at the third term, since the terms before powers of  $\frac{\lambda^2}{z}$ , which are functions of  $e$ , will be quite small for higher order terms.

The integrands in Eq. (35) become small when  $\lambda$  is large, and since  $\sqrt{2z} > 20$ , we can replace the limit  $\sqrt{2z}$  by  $\infty$  with a relative error of less than  $10^{-16}$  [26]. We also have the standard integrals

$$\int_0^\infty \exp(-\lambda^2) d\lambda = \frac{\sqrt{\pi}}{2}, \quad (36)$$

$$\int_0^\infty \lambda^2 \exp(-\lambda^2) d\lambda = \frac{\sqrt{\pi}}{4}, \quad (37)$$

$$\int_0^\infty \lambda^4 \exp(-\lambda^2) d\lambda = \frac{3\sqrt{\pi}}{8}. \quad (38)$$

By using these equations, the averaged value  $\bar{\rho v}$  in Eq. (35) can be obtained,

$$\begin{aligned}
\bar{\rho v} &\approx \sqrt{\frac{\mu(1 - e^2)}{2a\pi z}} \rho_{p0} \exp \left( \frac{r_{p0} - r_p}{H_p} \right) \\
&\left[ 1 + \frac{1 + 3e^2}{8z(1 - e^2)} + \frac{3(3 - 14e^2 - 5e^4)}{128z^2(1 - e^2)^2} \right]. \quad (39)
\end{aligned}$$

By using Eqs. (26), (27), (29), and (30), the averaged value  $\bar{\rho v \mathbf{v}}$  in Eq. (25) can be written as

$$\begin{aligned}
\bar{\rho v \mathbf{v}} &= \frac{1}{2\pi} \int_0^{2\pi} \rho v \mathbf{v} dM = \frac{\mu}{2\pi a} \rho_{p0} \exp \left( \frac{a_0 - a_0 e_0 - a}{H_p} \right) \\
&\left[ \int_0^{2\pi} \exp \left( z \cos E \right) \frac{\sqrt{1 + e \cos E}}{\sqrt{1 - e \cos E}} (-\sin E) dE \hat{\mathbf{e}} \right. \\
&\left. + \sqrt{1 - e^2} \int_0^{2\pi} \exp \left( z \cos E \right) \frac{\sqrt{1 + e \cos E}}{\sqrt{1 - e \cos E}} \cos E dE \hat{\mathbf{e}}_1 \right]. \quad (40)
\end{aligned}$$

Because

$$\int_0^{2\pi} \exp(z \cos E) \frac{\sqrt{1 + e \cos E}}{\sqrt{1 - e \cos E}} (-\sin E) dE = 0, \quad (41)$$

we have

$$\begin{aligned}
\bar{\rho v \mathbf{v}} &= \frac{\mu}{\pi a} \sqrt{1 - e^2} \rho_{p0} \exp \left( \frac{a_0 - a_0 e_0 - a}{H_p} \right) \\
&\left[ \int_0^\pi \exp \left( z \cos E \right) \frac{\sqrt{1 + e \cos E}}{\sqrt{1 - e \cos E}} \cos E dE \right] \hat{\mathbf{e}}_1. \quad (42)
\end{aligned}$$

With the same method used for calculating  $\bar{\rho v}$ , we also make the substitution  $\cos E = 1 - \frac{\lambda^2}{z}$  and expand integrands into powers of  $\frac{\lambda^2}{z}$ , and then

$$\begin{aligned}
\bar{\rho v \mathbf{v}} &= \frac{\mu}{\pi a} \left( 1 + e \right) \rho_{p0} \exp \left( \frac{r_{p0} - r_p}{H_p} \right) \sqrt{\frac{2}{z}} \times \int_0^{\sqrt{2z}} \exp(-\lambda^2) \\
&\left[ 1 + \frac{3e^2 - 4e - 3}{4(1 - e^2)} \frac{\lambda^2}{z} - \frac{5e^4 - 8e^3 - 26e^2 - 24e + 5}{32(1 - e^2)^2} \frac{\lambda^4}{z^2} + O \left( \frac{\lambda^6}{z^3} \right) \right] d\lambda \hat{\mathbf{e}}_1. \quad (43)
\end{aligned}$$

Here, the expansion is truncated at the third term due to the same reason as in Eq. (35).

Replacing the limit  $\sqrt{2z}$  by  $\infty$  and using Eqs. (36)–(38), the averaged value  $\bar{\rho v \mathbf{v}}$  in Eq. (43) can be obtained as

$$\begin{aligned}
\bar{\rho v \mathbf{v}} &\approx \frac{\mu(1 + e)}{a\sqrt{2z\pi}} \rho_{p0} \exp \left( \frac{r_{p0} - r_p}{H_p} \right) \\
&\left[ 1 + \frac{3e^2 - 4e - 3}{8z(1 - e^2)} - \frac{3(5e^4 - 8e^3 - 26e^2 - 24e + 5)}{128z^2(1 - e^2)^2} \right] \hat{\mathbf{e}}_1. \quad (44)
\end{aligned}$$

According to Eqs. (24), (25), (35), and (44), the averaged orbital dynamics of  $\mathbf{H}$  and  $\mathbf{e}$  under the atmospheric drag are given by

$$\dot{\mathbf{H}}_{Atm} = -\frac{1}{2} B \sqrt{\frac{\mu(1 - e^2)}{2a\pi z}} \rho_{p0} \exp \left( \frac{r_{p0} - r_p}{H_p} \right) (1 + K_1) \mathbf{H}, \quad (45)$$

$$\dot{\mathbf{e}}_{Atm} = -B \frac{1 + e}{a\sqrt{2\pi z}} \rho_{p0} \exp \left( \frac{r_{p0} - r_p}{H_p} \right) (1 + K_2) \mathbf{H} \hat{\mathbf{e}}, \quad (46)$$

where

$$K_1 = \frac{1 + 3e^2}{8z(1 - e^2)} + \frac{3(3 - 14e^2 - 5e^4)}{128z^2(1 - e^2)^2} \approx \frac{1 + 3e^2}{8z(1 - e^2)}, \quad (47)$$

$$\begin{aligned}
K_2 &= \frac{3e^2 - 4e - 3}{8z(1 - e^2)} - \frac{3(5e^4 - 8e^3 - 26e^2 - 24e + 5)}{128z^2(1 - e^2)^2} \\
&\approx \frac{3e^2 - 4e - 3}{8z(1 - e^2)}. \quad (48)
\end{aligned}$$

The approximations of  $K_1$  and  $K_2$  in Eqs. (47) and (48) are based on the fact that during the GTO evolution we have  $e < \approx 0.7$  and  $z \approx 290$ , and then the magnitudes of the second terms in Eqs. (47)

and (48) are always less than  $5.5 \times 10^{-6}$  and  $3 \times 10^{-5}$ , respectively, and can usually be neglected.

### 3.3. Resultant averaged orbital dynamics

According to Eqs. (13), (14), (45), and (46), the resultant singly-averaged orbital dynamics (SAOD) of  $\mathbf{H}$  and  $\mathbf{e}$  over the orbital motion on the GTO under  $J_2$ , luni-solar third-body perturbations, and atmospheric drag are given by

$$\begin{aligned}\dot{\mathbf{H}} &= \dot{\mathbf{H}}_{J_2} + \dot{\mathbf{H}}_S + \dot{\mathbf{H}}_M + \dot{\mathbf{H}}_{Atm} \\ &= -\frac{3\mu J_2 R_E^2}{2a^3 h^5} (\hat{\mathbf{p}} \cdot \mathbf{h}) \hat{\mathbf{p}}^\times \mathbf{h} + \frac{3a^2 \mu_S}{2d_S^3} \left[ 5(\hat{\mathbf{d}}_S \cdot \mathbf{e}) \mathbf{e}^\times \hat{\mathbf{d}}_S - (\hat{\mathbf{d}}_S \cdot \mathbf{h}) \mathbf{h}^\times \hat{\mathbf{d}}_S \right] \\ &\quad + \frac{3a^2 \mu_M}{2d_M^3} \left[ 5(\hat{\mathbf{d}}_M \cdot \mathbf{e}) \mathbf{e}^\times \hat{\mathbf{d}}_M - (\hat{\mathbf{d}}_M \cdot \mathbf{h}) \mathbf{h}^\times \hat{\mathbf{d}}_M \right] \\ &\quad - \frac{1}{2} B \sqrt{\frac{\mu(1-e^2)}{2a\pi z}} \rho_{p0} \exp\left(\frac{r_{p0} - r_p}{H_p}\right) (1 + K_1) \mathbf{H},\end{aligned}\quad (49)$$

$$\begin{aligned}\dot{\mathbf{e}} &= \dot{\mathbf{e}}_{J_2} + \dot{\mathbf{e}}_S + \dot{\mathbf{e}}_M + \dot{\mathbf{e}}_{Atm} \\ &= -\frac{3\mu J_2 R_E^2}{4a^2 h^5} \left\{ \left[ 1 - \frac{5}{h^2} (\hat{\mathbf{p}} \cdot \mathbf{h})^2 \right] \mathbf{h}^\times + 2(\hat{\mathbf{p}} \cdot \mathbf{h}) \hat{\mathbf{p}}^\times \right\} \mathbf{e} \\ &\quad + \frac{3\mu_S}{2nd_S^3} \left[ 5(\hat{\mathbf{d}}_S \cdot \mathbf{e}) \mathbf{h}^\times \hat{\mathbf{d}}_S - (\hat{\mathbf{d}}_S \cdot \mathbf{h}) \mathbf{e}^\times \hat{\mathbf{d}}_S - 2\mathbf{h}^\times \mathbf{e} \right] \\ &\quad + \frac{3\mu_M}{2nd_M^3} \left[ 5(\hat{\mathbf{d}}_M \cdot \mathbf{e}) \mathbf{h}^\times \hat{\mathbf{d}}_M - (\hat{\mathbf{d}}_M \cdot \mathbf{h}) \mathbf{e}^\times \hat{\mathbf{d}}_M - 2\mathbf{h}^\times \mathbf{e} \right] \\ &\quad - B \frac{1+e}{a\sqrt{2\pi z}} \rho_{p0} \exp\left(\frac{r_{p0} - r_p}{H_p}\right) (1 + K_2) H \hat{\mathbf{e}}.\end{aligned}\quad (50)$$

Notice that the bar operator is omitted from the Milankovitch elements  $\mathbf{H}$  and  $\mathbf{e}$  in Eqs. (49) and (50) and in what follows, because there is no ambiguity, i.e., all elements are averaged.

Similarly, according to Eqs. (15), (16), (45), and (46), the resultant doubly-averaged orbital dynamics of  $\mathbf{H}$  and  $\mathbf{e}$  with the averaging performed over the GTO orbital motion and the motion of the Moon (DAOD) are given by

$$\begin{aligned}\dot{\mathbf{H}} &= \dot{\mathbf{H}}_{J_2} + \dot{\mathbf{H}}_S + \dot{\mathbf{H}}_M + \dot{\mathbf{H}}_{Atm} \\ &= -\frac{3\mu J_2 R_E^2}{2a^3 h^5} (\hat{\mathbf{p}} \cdot \mathbf{h}) \hat{\mathbf{p}}^\times \mathbf{h} \\ &\quad + \frac{3a^2 \mu_S}{2d_S^3} \left[ 5(\hat{\mathbf{d}}_S \cdot \mathbf{e}) \mathbf{e}^\times \hat{\mathbf{d}}_S - (\hat{\mathbf{d}}_S \cdot \mathbf{h}) \mathbf{h}^\times \hat{\mathbf{d}}_S \right] \\ &\quad - \frac{3a^2 \mu_M}{4a_M^3 h_M^3} \left[ 5(\hat{\mathbf{H}}_M \cdot \mathbf{e}) \mathbf{e}^\times \hat{\mathbf{H}}_M - (\hat{\mathbf{H}}_M \cdot \mathbf{h}) \mathbf{h}^\times \hat{\mathbf{H}}_M \right] \\ &\quad - \frac{1}{2} B \sqrt{\frac{\mu(1-e^2)}{2a\pi z}} \rho_{p0} \exp\left(\frac{r_{p0} - r_p}{H_p}\right) (1 + K_1) \mathbf{H},\end{aligned}\quad (51)$$

$$\begin{aligned}\dot{\mathbf{e}} &= \dot{\mathbf{e}}_{J_2} + \dot{\mathbf{e}}_S + \dot{\mathbf{e}}_M + \dot{\mathbf{e}}_{Atm} \\ &= -\frac{3\mu J_2 R_E^2}{4a^2 h^5} \left\{ \left[ 1 - \frac{5}{h^2} (\hat{\mathbf{p}} \cdot \mathbf{h})^2 \right] \mathbf{h}^\times + 2(\hat{\mathbf{p}} \cdot \mathbf{h}) \hat{\mathbf{p}}^\times \right\} \mathbf{e} \\ &\quad + \frac{3\mu_S}{2nd_S^3} \left[ 5(\hat{\mathbf{d}}_S \cdot \mathbf{e}) \mathbf{h}^\times \hat{\mathbf{d}}_S - (\hat{\mathbf{d}}_S \cdot \mathbf{h}) \mathbf{e}^\times \hat{\mathbf{d}}_S - 2\mathbf{h}^\times \mathbf{e} \right] \\ &\quad - \frac{3\mu_M}{4na_M^3 h_M^3} \left[ 5(\hat{\mathbf{H}}_M \cdot \mathbf{e}) \mathbf{h}^\times \hat{\mathbf{H}}_M - (\hat{\mathbf{H}}_M \cdot \mathbf{h}) \mathbf{e}^\times \hat{\mathbf{H}}_M - 2\mathbf{h}^\times \mathbf{e} \right] \\ &\quad - B \frac{1+e}{a\sqrt{2\pi z}} \rho_{p0} \exp\left(\frac{r_{p0} - r_p}{H_p}\right) (1 + K_2) H \hat{\mathbf{e}}.\end{aligned}\quad (52)$$

In the same way, according to Eqs. (17), (18), (45), and (46), the resultant triply-averaged orbital dynamics of  $\mathbf{H}$  and  $\mathbf{e}$  with the averaging performed over the GTO orbital motion and the motions of the Moon and Sun (TAOD) are given by

$$\begin{aligned}\dot{\mathbf{H}} &= \dot{\mathbf{H}}_{J_2} + \dot{\mathbf{H}}_S + \dot{\mathbf{H}}_M + \dot{\mathbf{H}}_{Atm} \\ &= -\frac{3\mu J_2 R_E^2}{2a^3 h^5} (\hat{\mathbf{p}} \cdot \mathbf{h}) \hat{\mathbf{p}}^\times \mathbf{h} - \frac{3a^2 \mu_S}{4a_S^3 h_S^3} \left[ 5(\hat{\mathbf{H}}_S \cdot \mathbf{e}) \mathbf{e}^\times \hat{\mathbf{H}}_S - (\hat{\mathbf{H}}_S \cdot \mathbf{h}) \mathbf{h}^\times \hat{\mathbf{H}}_S \right] \\ &\quad - \frac{3a^2 \mu_M}{4a_M^3 h_M^3} \left[ 5(\hat{\mathbf{H}}_M \cdot \mathbf{e}) \mathbf{e}^\times \hat{\mathbf{H}}_M - (\hat{\mathbf{H}}_M \cdot \mathbf{h}) \mathbf{h}^\times \hat{\mathbf{H}}_M \right] \\ &\quad - \frac{1}{2} B \sqrt{\frac{\mu(1-e^2)}{2a\pi z}} \rho_{p0} \exp\left(\frac{r_{p0} - r_p}{H_p}\right) (1 + K_1) \mathbf{H},\end{aligned}\quad (53)$$

$$\begin{aligned}\dot{\mathbf{e}} &= \dot{\mathbf{e}}_{J_2} + \dot{\mathbf{e}}_S + \dot{\mathbf{e}}_M + \dot{\mathbf{e}}_{Atm} \\ &= -\frac{3\mu J_2 R_E^2}{4a^2 h^5} \left\{ \left[ 1 - \frac{5}{h^2} (\hat{\mathbf{p}} \cdot \mathbf{h})^2 \right] \mathbf{h}^\times + 2(\hat{\mathbf{p}} \cdot \mathbf{h}) \hat{\mathbf{p}}^\times \right\} \mathbf{e} \\ &\quad - \frac{3\mu_S}{4na_S^3 h_S^3} \left[ 5(\hat{\mathbf{H}}_S \cdot \mathbf{e}) \mathbf{h}^\times \hat{\mathbf{H}}_S - (\hat{\mathbf{H}}_S \cdot \mathbf{h}) \mathbf{e}^\times \hat{\mathbf{H}}_S - 2\mathbf{h}^\times \mathbf{e} \right] \\ &\quad - \frac{3\mu_M}{4na_M^3 h_M^3} \left[ 5(\hat{\mathbf{H}}_M \cdot \mathbf{e}) \mathbf{h}^\times \hat{\mathbf{H}}_M - (\hat{\mathbf{H}}_M \cdot \mathbf{h}) \mathbf{e}^\times \hat{\mathbf{H}}_M - 2\mathbf{h}^\times \mathbf{e} \right] \\ &\quad - B \frac{1+e}{a\sqrt{2\pi z}} \rho_{p0} \exp\left(\frac{r_{p0} - r_p}{H_p}\right) (1 + K_2) H \hat{\mathbf{e}}.\end{aligned}\quad (54)$$

The terms related to the Moon and Sun in the averaged orbital dynamics, i.e.,  $\mathbf{d}_S$ ,  $\mathbf{d}_M$ ,  $\mathbf{H}_S$ , and  $\mathbf{H}_M$ , can either be provided by an ephemeris or given by a two-body solution.

## 4. Orbital dynamics model verification

To verify the averaged orbital models (49)–(54), a numerical simulation is carried out and compared with HPOP and LOP. Important dynamical properties of the GTO are revealed this way.

### 4.1. Initial conditions and system parameters setting

The epoch is set to be 1 January 2015 00:00:00 UTC, and the orbits will be propagated for 10 years. The initial orbital elements of the GTO, defined at injection, are chosen as the typical mission profile of Ariane 5 (launched from Kourou),

$$h_{a0} = 35,943 \text{ km}, \quad h_{p0} = 250 \text{ km}, \quad i_0 = 6^\circ, \quad \omega_0 = 178^\circ, \quad (55)$$

where  $h_{a0}$  and  $h_{p0}$  are the initial values of the apogee height and

**Table 1**  
Atmospheric density  $\rho_{p0}$  and scale height  $H_p$  in the exponential model with different  $h_{p0}$ .

Initial perigee height $h_{p0}$ (km)	Atmospheric density $\rho_{p0}$ (kg/m <sup>3</sup> )	Scale height $H_p$ (km)
200	$2.54097 \times 10^{-10}$	38.70
250	$7.28754 \times 10^{-11}$	41.38
300	$2.26738 \times 10^{-11}$	44.37
350	$7.65299 \times 10^{-12}$	47.82
400	$2.80220 \times 10^{-12}$	51.87
500	$4.79651 \times 10^{-13}$	62.40

perigee height, respectively.<sup>4</sup> The initial RAAN and mean anomaly are chosen as

$$\Omega_0 = 60^\circ, \quad M_0 = 0^\circ. \quad (56)$$

Notice that the solar radiation pressure (SRP) is taken into account in HPOP and LOP but not in the orbital models (49)–(54), and the exponential density model is simpler than those in HPOP and LOP. To be more conservative in the model verification, we choose a higher AMR, which implies more significant effects of SRP and atmospheric drag. Therefore,

$$S/m = 0.02 \text{ m}^2/\text{kg}, \quad C_D = 2.2. \quad (57)$$

The exponential atmospheric density model (21) adopted in our orbital models needs the density  $\rho_{p0}$  at the initial perigee  $r_{p0}$  and the constant scale height  $H_p$ , both of which can be given based on the 1976 U.S. Standard Atmosphere Model (USSA76). The atmospheric density at the altitude  $h_x$  between 200 km and 600 km in USSA76 can be approximated by the curve

$$\log_{10}[\rho(h_x)] = 7.0725 \times 10^{-6}(h_x - 200)(h_x - 400) - 9.7875 \times 10^{-3}(h_x - 200) - 9.595, \quad (58)$$

where the altitude  $h_x$  is in unit of km, and the atmospheric density  $\rho(h_x)$  is given in unit of kg/m<sup>3</sup>.

In what follows, the atmospheric density  $\rho_{p0}$  at the initial perigee  $r_{p0}$  in Eq. (21) will be as in Eq. (58), and the constant scale height  $H_p$  in Eq. (21) will be set as the local scale height at the initial perigee  $r_{p0}$ , which can be calculated by using Eq. (58),

$$H_{p-Local}(h_x) = - \frac{1}{\log_e(10) \left( 1.4145 \times 10^{-5} h_x - 5.544 \times 10^{-3} \right)}, \quad (59)$$

where the altitude  $h_x$  and local scale height  $H_{p-Local}$  both have units of km. The atmospheric density  $\rho_{p0}$  at the initial perigee and the scale height  $H_p$  for different values of  $h_{p0}$  are listed in Table 1.

As for the luni-solar perturbations, both the orbits of the Moon and Sun are assumed circular, and the lunar orbit is assumed to be within the ecliptic plane, that is, neglecting the 5-degree angle between the lunar orbital plane and the ecliptic plane, as well as the lunar orbit precession. With the luni-solar argument of latitude at epoch already known, the luni-solar positions  $\mathbf{d}_M$  and  $\mathbf{d}_S$  can be generated by using the above assumption.

The HPOP in STK is used to generate a precise orbit ephemeris. In the simulation, the force model in HPOP includes the gravity of Earth ( $21 \times 21$  spherical harmonics model EGM96), luni-solar third-body gravity, and atmospheric drag (Jacchia–Roberts atmospheric density model with AMR and drag coefficient given by Eq. (57)), and also includes SRP (spherical SRP model with AMR given by Eq. (57) and SRP coefficient  $C_r = 1.5$ ).

The LOP in STK allows prediction of a satellite's orbit over years. The LOP exploits averaging over the satellite's orbital motion, similar to the SAOD in Eqs. (49) and (50). In the simulation, the force model in LOP includes the gravity of Earth ( $12 \times 12$  spherical harmonics model), luni-solar gravity and atmospheric drag (USSA76 atmospheric density model with AMR and drag coefficient given by Eq. (57)), and also includes SRP (AMR is given by Eq. (57) and SRP coefficient  $C_r = 1.5$ ).

King-Hele [26] pointed out that satellite orbits in the atmosphere usually end when the perigee height has dropped to between 120 km and 150 km. According to actual observation data from Fairbanks, Alaska, Janin and Roth [18] showed that after reaching an altitude of 120 km HEOS-1 began its deceleration phase, and three minutes later the volatilization of major parts of the satellite occurred at an altitude of 50 km. Another consideration is the validity of the free molecular flow theory. Free molecular flow can only exist when the mean free path of molecules is larger than twice the maximum length or diameter of the satellite. The mean free path increases from about 2 m at a height of 120 km to about 50 m at a height of 160 km [26]. Therefore, for a rocket upper stage, the free molecular flow theory will not be rigorous at low altitudes. Because of these facts, when the perigee height of the GTO is lower than 120 km, the upper stage can be regarded burnt, the GTO can be regarded to have decayed, and the simulation is stopped. To be more conservative in the aspect of orbital debris decay, we will set the critical perigee height to 100 km instead of 120 km.

The ODE4 (Runge–Kutta) integrator in Simulink is used for the SAOD, DAOD, and TAOD. The time step of the simulations for SAOD, DAOD, and TAOD is 10,000 s, while the time steps of HPOP and LOP are 49 s and 1 day, respectively. For SAOD, DAOD, and TAOD, we have tested the time steps 1000 s, 10,000 s, and 100,000 s (about 1 day). It was found that the simulation results in the cases of 10,000 s and 100,000 s has slight differences, whereas those in the cases of 1000 s and 10,000 are almost the same. Therefore, 10,000 s is finally chosen as the time step.

#### 4.2. Simulation results

The orbital elements of interest are the semi-major axis  $a$ , eccentricity  $e$ , and perigee height  $h_p = a(1 - e) - R_E$ . Time histories of  $a$ ,  $e$ , and  $h_p$  propagated by our orbital models, HPOP, and LOP are given in Figs. 1–3, respectively.

The SAOD model agrees quite well with HPOP within the first

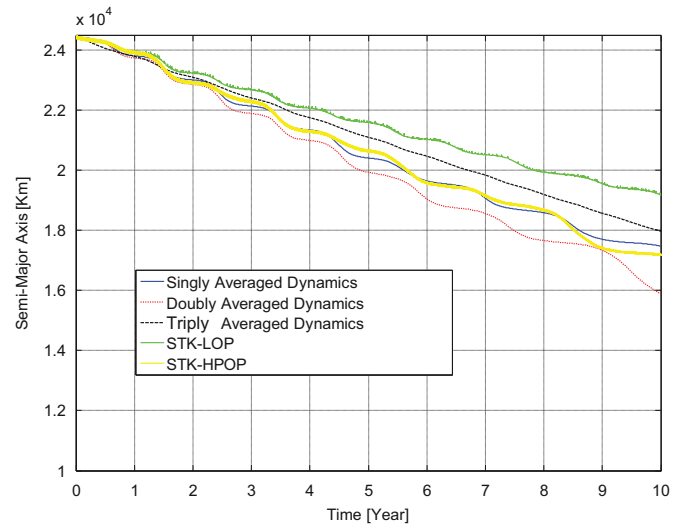


**Fig. 1.** Time history of the semi-major axis  $a$ .

<sup>4</sup> Ariane 5 User's Manual, Issue 5, Revision 1, July 2011.



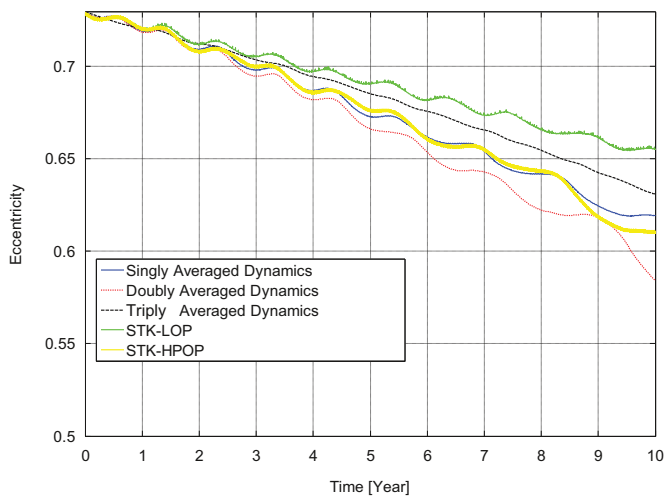


Fig. 2. Time history of the eccentricity  $e$ .

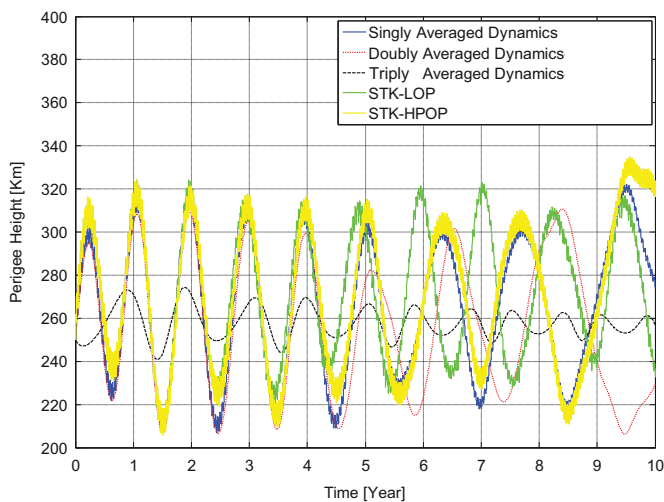


Fig. 3. Time history of the perigee height  $h_p$ .

nine years. However, after the ninth year, the SAOD model starts to diverge away from HPOP due to the 1:1 solar apsidal resonance between the solar motion and the precession of the apsidal line caused by the Earth oblateness. This resonance keeps a nearly constant Sun azimuth for a relatively long duration, and the solar perturbation raises the perigee height, as shown by Fig. 3. The DAOD model has a lower precision than SAOD, since, as shown by Fig. 3, it neglects the 14-day perigee height oscillation induced by the lunar orbital motion, which influences the atmospheric drag. The TAOD model has the lowest precision among our three models, since it neglects the 180-day perigee height oscillation induced by the solar orbital motion, which has an amplitude of about 50 km, much larger than that of the 14-day oscillation, as shown by Fig. 3.

No averaging process has been performed in HPOP, so, the orbit contains high-frequency oscillations, which are short-period terms associated with the GTO orbital motion. LOP exploits the averaging process over the orbital motion on the GTO, similar to the SAOD, so the orbits by LOP and SAOD contain the short-period terms induced by the luni-solar orbital motions and the long-period terms. DAOD exploits the averaging process over the lunar orbital motion, so it does not contain the 14-day short-period term. TAOD, which has been averaged over the luni-solar orbital motions and does not contain short-period terms, is the most different among all the models, since the 180-day short-period term with an amplitude of

about 50 km has been eliminated. The long-period term induced by the luni-solar orbital momenta, which has a period of about 1–2 years, can be seen in TAOD. According to Figs. 1 and 2, the reduction rates of  $a$  and  $e$  of different models are different, and this is mainly caused by their different perigee height oscillations.

Consequently, the SAOD model can capture the main effects of the perturbations quite well in a ten-year time span. Therefore, the SAOD model can be used for a computationally-efficient orbit propagation in a time span of several years. Although with a lower precision, the doubly-averaged orbital model DAOD and the triply-averaged orbital model TAOD can depict the general orbital evolution and will perform better for a higher initial perigee.

## 5. Lifetime reduction using luni-solar perturbations

The orbital lifetime of the GTO is determined by both the decaying effect of atmospheric drag and the perigee height (eccentricity) oscillation caused by the luni-solar perturbations. In this section, we will focus on the GTO lifetime reduction by using the luni-solar perturbations. Several previous works studied the effect of the luni-solar perturbations on the GTO lifetime, such as Refs. [4–8]. Compared with the previous works, the study here will provide an analytical insight of the problem, show the underlying mechanism more clearly, and give a more direct relation between the effect of the luni-solar perturbations and the orbital geometry. Finally, the desired initial orbital geometry is given, with which the orbital lifetime can be reduced to the maximum extent in the statistical sense. Here, one should keep in mind that due to the chaotic nature of the decay dynamics of GTOs caused by the solar apsidal resonance, the orbital lifetime of GTOs is actually a statistical problem, and a lower perigee height can increase the probability of atmospheric re-entry within a given time limit [7,8]. This is exactly what the term “statistical sense” means.

### 5.1. Underlying mechanism

As stated before, through the perigee height oscillation, the luni-solar perturbations can reduce or enhance the orbital lifetime of the GTO remarkably. Here we consider one extreme case of the orbital lifetime reduction: if the long-period perigee height oscillation is initially at the beginning of a decrease phase, the long-period perigee height will oscillate always below the initial perigee height; if the short-period oscillation is also initially at the beginning of a decrease phase, the short-period perigee height will oscillate with the long-period oscillation as its upper envelope; consequently, the superposition will be always below the initial perigee height, and the maximum distance from the initial perigee will be twice the sum of amplitudes of the oscillations. In this case, both the long- and short-period perturbations are fully utilized to lower the perigee height. The effect of atmospheric drag will be the strongest, and the orbital lifetime will be reduced to the maximum extent in the statistical sense.

As stated in Section 1, the initial phase of the long-period oscillation is determined by the initial relative geometry of the luni-solar orbital (ecliptic) plane with respect to the GTO apsidal line, while the initial phases of the 14-day and 180-day short-period oscillations are determined by the initial azimuths of the Moon and Sun with respect to the GTO apsidal line, respectively. According to Section 4, the amplitude of the short-period perigee height oscillation induced by the lunar motion for the GTO is only about 3 km and, thus, has a small influence. Therefore, we will only consider the solar gravity; i.e., we will choose the proper initial orbital geometry with respect to the ecliptic plane and the Sun for the desired initial phases of the eccentricity oscillations.

## 5.2. Initial orbital geometry via launch date and hour

The desired initial orbital geometry of the GTO can be achieved through a proper launch date and launch hour. For the GTO missions launched by a launch vehicle with a fixed launch site, the typical mission profile is usually defined, and the optimal injection conditions of the GTO are obtained in the mission profile and are usually fixed. Thus, initial values of some orbital elements of the GTO at injection are known. For example, the optimized standard GTO launched by Ariane 5 from Kourou, defined in terms of orbital elements at injection, is given by Eq. (55). The only orbital element that is left free is  $\Omega$ , which is determined by the launch time.

The desired initial relative geometry of the ecliptic plane with respect to the GTO apsidal line can be achieved by choosing the proper initial  $\Omega$ . With  $\Omega$  set, the orientation of the GTO is known, and the desired initial azimuth of the Sun with respect to the GTO apsidal line can be achieved by choosing the proper launch date. With  $\Omega$  and the launch date known, the launch hour can be determined. Notice that the analyses herein are performed only from the perspective of the GTO lifetime reduction, but in reality the launch date and hour are subjected to other constrains. In the following discussion, we will focus on finding the desired initial orbital geometry and will not consider the corresponding launch date and hour.

## 5.3. Desired initial orbital geometry

### 5.3.1. Long-period oscillation

According to the averaged orbital dynamics (54), the triply-averaged variational equation of  $\mathbf{e}$  under the solar perturbation, which only contains the long-period oscillation, can be written as

$$\dot{\mathbf{e}}_s = -\frac{3\mu_s}{4na_s^3h_s^3} \left[ 5(\hat{\mathbf{H}}_s \cdot \mathbf{e}) \mathbf{h} \times \hat{\mathbf{H}}_s - (\hat{\mathbf{H}}_s \cdot \mathbf{h}) \mathbf{e} \times \hat{\mathbf{H}}_s - 2\mathbf{h} \times \mathbf{e} \right], \quad (60)$$

where we have

$$\hat{\mathbf{H}}_s = [0 \quad -\sin(i_s) \quad \cos(i_s)]^T,$$

$$\mathbf{e} = e [\cos \omega \cos \Omega - \sin \omega \cos i \sin \Omega, \cos \omega \sin \Omega + \sin \omega \cos i \cos \Omega, \sin \omega \sin i]^T$$

$$\mathbf{h} = \sqrt{1-e^2} [\sin \Omega \sin i, -\cos \Omega \sin i, \cos i]^T.$$

Substituting these equations into Eq. (60), another form of Eq. (60) formulated in terms of classical orbital elements, which is somewhat tedious, can be given.

Notice that only the magnitude of  $\mathbf{e}$ , i.e., the eccentricity  $e$ , affects the perigee height. The second and third terms in Eq. (60) are perpendicular to  $\mathbf{e}$ , and will not contribute to a change of  $e$ . Taking the dot product of both sides of Eq. (60) with the unit vector  $\hat{\mathbf{e}}$  yields the long-period change rate of  $e$  caused by the solar perturbation,

$$\dot{e}_s = -\frac{15\mu_s}{4na_s^3h_s^3} (\hat{\mathbf{H}}_s \cdot \mathbf{e}) (\mathbf{h} \times \hat{\mathbf{H}}_s) \cdot \hat{\mathbf{e}}. \quad (61)$$

Since  $\mathbf{H}_s$  is constant, the long-period oscillation of  $e$  in Eq. (61) is induced by the periodic motions of  $\mathbf{e}$  and  $\mathbf{h}$ , where  $h = \sqrt{1-e^2}$ , which are mainly caused by the Earth oblateness. The time rates of  $\Omega$  and  $\omega$  caused by  $J_2$  are

$$\dot{\Omega}_{J_2} = -1.5J_2 \sqrt{\mu} R_E^2 \frac{\cos i}{a^{7/2}(1-e^2)^2}, \quad (62)$$

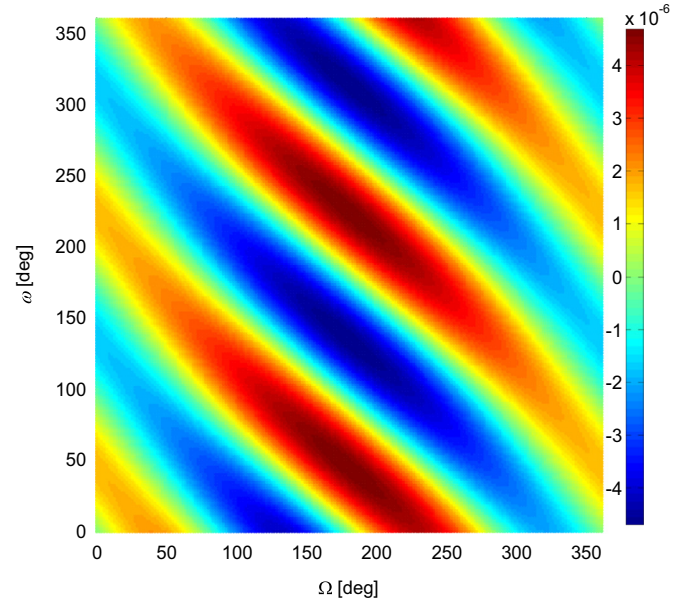


Fig. 4. Long-period eccentricity change per day with  $i=6^\circ$ .

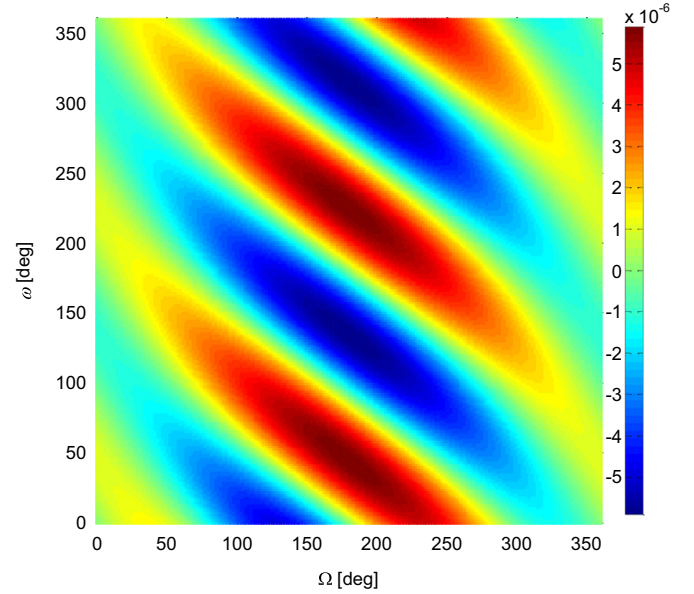


Fig. 5. Long-period eccentricity change per day with  $i=10^\circ$ .

$$\dot{\omega}_{J_2} = 0.75J_2 \sqrt{\mu} R_E^2 \frac{5\cos^2 i - 1}{a^{7/2}(1-e^2)^2}. \quad (63)$$

For GTOs with  $0^\circ \leq i < 30^\circ$ , we always have  $\dot{\Omega}_{J_2} < 0$  and  $\dot{\omega}_{J_2} > 0$ .

To investigate the long-period eccentricity change caused by the solar third-body perturbation, we plot the long-period eccentricity change per day with respect to  $\Omega$  and  $\omega$  for different inclinations  $i=6^\circ, 10^\circ, 23^\circ, 26^\circ, 30^\circ, 40^\circ$  using  $\dot{e}_s$  in Eq. (61), as shown in Figs. 4–8. The apogee height and perigee height are chosen as the standard GTO launched by Ariane 5 in Eq. (55).

According to Figs. 4–8, the long-period eccentricity change caused by the solar third-body perturbation has an evident pattern with respect to  $\Omega$  and  $\omega$ . We can draw several conclusions:

1. Among all the values of  $\Omega$ , the long-period solar perturbation is strongest at  $\Omega = 180^\circ$  and weakest at  $\Omega = 0^\circ$ . Notice that at

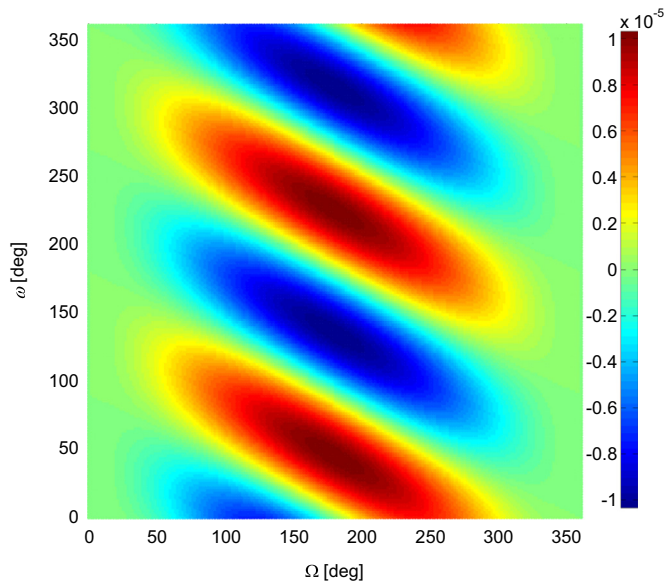


Fig. 6. Long-period eccentricity change per day with  $i=23^{\circ}26'$ .

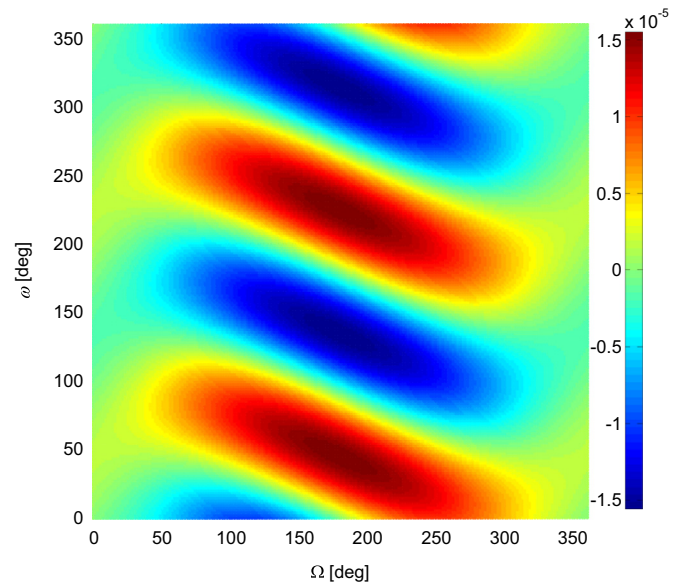


Fig. 8. Long-period eccentricity change per day with  $i=40^{\circ}$ .

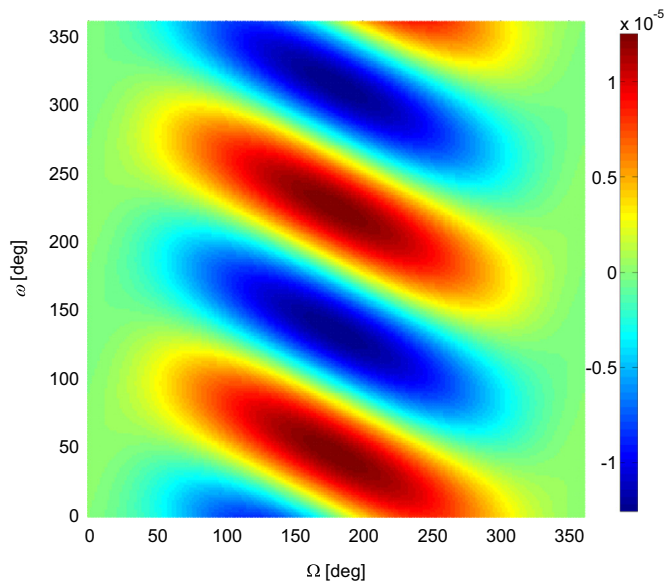


Fig. 7. Long-period eccentricity change per day with  $i=30^{\circ}$ .

$\Omega = 180^{\circ}$ , the declination of  $\mathbf{H}_S$  with respect to the orbital plane of the GTO is minimum, equal to  $66^{\circ}34' - i$ , while at  $\Omega = 0^{\circ}$  the declination of  $\mathbf{H}_S$  is maximum, equal to  $90^{\circ} - |23^{\circ}26' - i|$ . Therefore, the magnitude of the long-period solar perturbation is determined by the declination of  $\mathbf{H}_S$ ; the perturbation is more significant with a smaller declination. This can also be seen in Eq. (61).

- When the GTO has the same inclination as the ecliptic plane, i.e.,  $i = 23^{\circ}26'$ , at  $\Omega = 0^{\circ}$  the maximum declination of  $\mathbf{H}_S$  is  $90^{\circ}$ . Then, at  $\Omega = 0^{\circ}$ , the inclination  $i = 23^{\circ}26'$  has the weakest long-period solar perturbation among all the inclinations; actually, according to Eq. (61),  $\dot{e}_S = 0$  at  $\{\Omega = 0^{\circ}, i = 23^{\circ}26'\}$ .
- As shown by Figs. 4–8, as the inclination increases, at  $\Omega = 180^{\circ}$ , the minimum declination of  $\mathbf{H}_S$  becomes smaller. Therefore, the long-period solar perturbation becomes more significant; the maximum long-period eccentricity change per day in Fig. 4 with  $i=6^{\circ}$  is about  $4 \times 10^{-6}$ , while this value in Fig. 8 with  $i=40^{\circ}$  is about  $1.5 \times 10^{-5}$ , four times larger than in the case of  $i=6^{\circ}$ .
- The phase of the long-period solar perturbation is determined

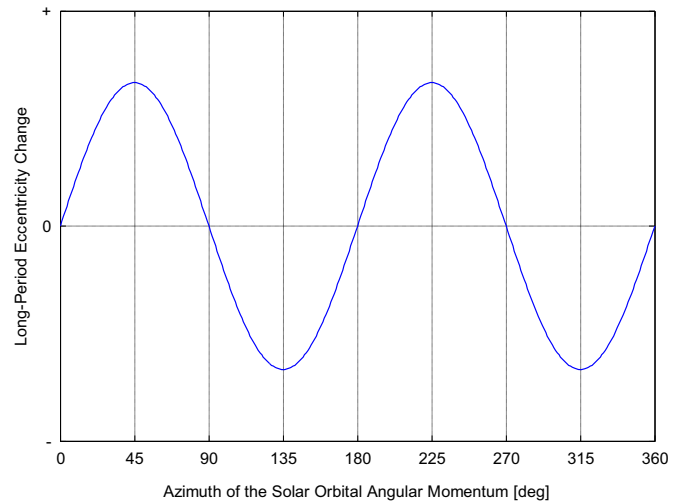


Fig. 9. Approximation of the phase of the long-period solar perturbation with respect to the azimuth of  $\mathbf{H}_S$  at a given  $\Omega$ .

by the azimuth of  $\mathbf{H}_S$  with respect to the GTO apsidal line. Here, the positive direction of the azimuth is defined to be the same as that of the true anomaly of the GTO. As shown by Figs. 4–8, with  $\Omega$  fixed, as  $\omega$  increases from  $0^{\circ}$  to  $360^{\circ}$ , i.e., as the azimuth of  $\mathbf{H}_S$  decreases by  $2\pi$ , the long-period eccentricity change goes through two periods. According to Eq. (61), during these two periods, when the azimuth of  $\mathbf{H}_S$  is  $0, \pi/2, \pi, 3\pi/2$ , and  $2\pi$ , the eccentricity change is zero. Also notice the sign of the eccentricity change in Figs. 4–8, the phase of the long-period solar perturbation with respect to the azimuth of  $\mathbf{H}_S$  can be represented approximately by a trigonometric function, as shown by Fig. 9.

- As stated above, as for the long-period perturbation of the solar third-body gravity, its magnitude and phase are determined by the declination of  $\mathbf{H}_S$  with respect to the GTO orbital plane and the azimuth of  $\mathbf{H}_S$  with respect to the GTO apsidal line, respectively.

To use above results to obtain the desired initial orbital geometry for lifetime reduction, we note that the long-period evolution of the eccentricity under the solar third-body gravity is



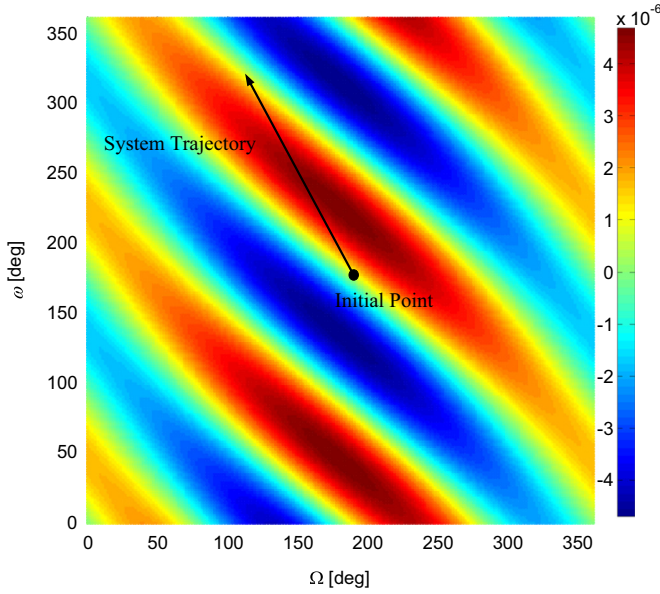


Fig. 10. Roughly estimated trajectory in the  $\Omega$ - $\omega$  plane.

determined not only by the distribution of the eccentricity change rate in Figs. 4–8 but also by the trajectory of the system in the  $\Omega$ - $\omega$  plane. That is to say, the long-period evolution of the eccentricity is the time integral of the eccentricity change rate along the system trajectory in the  $\Omega$ - $\omega$  plane. Along the system trajectory, the magnitude of the long-period solar perturbation will change with  $\Omega$ , but the phase in Fig. 9 will be unchanged. Since the orbital precession is mainly caused by  $J_2$ , by using Eqs. (62) and (63), the trajectory in the  $\Omega$ - $\omega$  plane can be roughly estimated as a strange line,

$$\frac{\omega - \omega_0}{\Omega - \Omega_0} \approx \frac{\dot{\omega}_{J_2}}{\dot{\Omega}_{J_2}} = -\frac{5\cos^2 i - 1}{2\cos i}. \quad (64)$$

As stated before, to reduce the orbital lifetime by the luni-solar perturbations, it is desired that the long-period oscillation of the perigee height is initially at the beginning of a decrease phase, that is, the oscillation of the eccentricity is initially at the beginning of an increase phase. To guarantee this condition, (since  $\dot{\omega} > 0$ , then the azimuth will continuously decrease accordingly), we want the initial azimuth of  $\hat{\mathbf{H}}_5$  to be about  $90^\circ$  or  $270^\circ$ , as shown in Fig. 9.

Take the optimized standard GTO launched by Ariane 5 in Eq. (55) as an example; the approximated trajectory in the  $\Omega$ - $\omega$  plane is

$$\frac{\omega - \omega_0}{\Omega - \Omega_0} = -\frac{5\cos^2 i - 1}{2\cos i} = -1.9836. \quad (65)$$

The desired initial orbital geometry: as shown by Fig. 10, since  $\omega_0 = 178^\circ$ , if we set  $\Omega_0 = 195^\circ$ , the initial azimuth of  $\hat{\mathbf{H}}_5$  is about  $270^\circ$ , the trajectory of the system will first go through an eccentricity raise, i.e., the long-period oscillation of the eccentricity is initially at the beginning of an increase phase.

### 5.3.2. Short-period oscillation

The desired initial orbital geometry for the long-period perturbation alone is not enough for the orbital lifetime reduction, since the short-period oscillation induced by the solar orbital motion has a larger amplitude than the long-period oscillation, as shown in Section 4. Therefore, the short-period oscillation of the perigee height is also required to be initially at the beginning of a decrease, and then the short-period perigee height will have the

long-period perigee as its upper envelope.

According to the averaged orbital dynamics Eq. (50), the singly-averaged variational equation of  $\mathbf{e}$  under the solar perturbation, which contains the long-period and the 180-day short-period oscillations, can be written as

$$\dot{\mathbf{e}}_s = \frac{3\mu_s}{2nd_s^3} \left[ 5(\hat{\mathbf{d}}_s \cdot \mathbf{e}) \mathbf{h} \times \hat{\mathbf{d}}_s - (\hat{\mathbf{d}}_s \cdot \mathbf{h}) \mathbf{e} \times \hat{\mathbf{d}}_s - 2\mathbf{h} \times \mathbf{e} \right]. \quad (66)$$

Obviously, the second and third terms in Eq. (66) will not contribute to the change of  $e$ . Taking a dot product of both sides of Eq. (66) with the unit vector  $\hat{\mathbf{e}}$  yields the time rate of the long- and short-period eccentricity change caused by the solar third-body perturbation,

$$\dot{e}_s = \frac{15\mu_s}{2nd_s^3} (\hat{\mathbf{d}}_s \cdot \mathbf{e}) (\mathbf{h} \times \hat{\mathbf{d}}_s) \cdot \hat{\mathbf{e}}. \quad (67)$$

The long- and short-period perturbations can be isolated and studied separately. Notice that the motion of the solar position vector  $\hat{\mathbf{d}}_s$  is faster than that of  $\mathbf{e}$  and  $\mathbf{h}$ , which are mainly caused by  $J_2$ . The effects of the periodic motion of  $\mathbf{e}$  and  $\mathbf{h}$  have already been taken into account in the long-period oscillation; therefore, here we assume that the vectors  $\mathbf{e}$  and  $\mathbf{h}$  are fixed and we only consider the short-period oscillation of  $e$  in Eq. (67) induced by the periodic motion of  $\hat{\mathbf{d}}_s$ .

Notice that the geometry in Eq. (67) is actually the same as that in Eq. (61): just replace  $\hat{\mathbf{H}}_5$  with  $\hat{\mathbf{d}}_s$  and put the opposite sign. Therefore, the conclusions on the long-period perturbation in Section 5.3.1 are also applicable to the short-period perturbation. Then, we can have the following conclusions on the short-period perturbation:

1. As for the short-period perturbation of the solar third-body gravity, its magnitude and phase are determined by the declination of  $\hat{\mathbf{d}}_s$  with respect to the GTO orbital plane and the azimuth of  $\hat{\mathbf{d}}_s$  with respect to the GTO apsidal line, respectively.
2. With a smaller declination of  $\hat{\mathbf{d}}_s$ , the short-period solar perturbation is more significant. Given  $\mathbf{e}$  and  $\mathbf{h}$ , with the solar orbital motion, the declination of  $\hat{\mathbf{d}}_s$  is changing periodically with zero as its minimum, and the perturbation magnitude can be assessed by the maximum declination. For the GTO with the inclination  $0-40^\circ$ , we can see that among all the values of  $\Omega$ , at  $\Omega = 0^\circ$  the maximum declination is the smallest, equal to  $123^\circ 26' - i$ , and at  $\Omega = 180^\circ$  the maximum declination is the

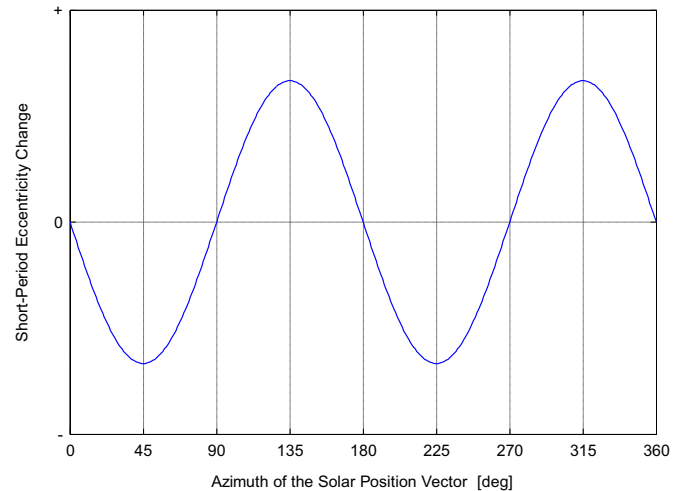


Fig. 11. Approximation of the phase of the short-period solar perturbation with respect to the azimuth of  $\hat{\mathbf{d}}_s$ .

largest, equal to  $23^\circ 26' + i$ . Therefore, opposite to the long-period perturbation, the short-period solar perturbation is strongest at  $\Omega = 0^\circ$  and weakest at  $\Omega = 180^\circ$ .

3. When the GTO has the same inclination as the ecliptic plane, i.e.,  $i = 23^\circ 26'$ , at  $\Omega = 0^\circ$  the declination of  $\hat{\mathbf{d}}_S$  is  $0^\circ$ . Therefore, the short-period solar perturbation is the strongest when the GTO orbital plane is within the ecliptic plane.
4. The phase of the short-period solar perturbation is determined by the azimuth of  $\hat{\mathbf{d}}_S$ . Because of the opposite sign, the approximated phase of the short-period perturbation with respect to the azimuth of  $\hat{\mathbf{d}}_S$  is opposite to that of the long-period perturbation in Fig. 9, as shown in Fig. 11.

As stated before, to reduce the orbital lifetime by the luni-solar perturbations, it is desired that the eccentricity oscillation is initially at the beginning of an increase phase. Noticing that the azimuth of  $\mathbf{d}_S$  will continuously increase with the solar orbital motion, we want the initial azimuth of  $\mathbf{d}_S$  to be about  $90^\circ$  or  $270^\circ$ , as shown in Fig. 11. That is, a short lifetime is obtained for the 6 h and 18 h local perigee time, and a long lifetime is obtained for the 12 h and 24 h local perigee time, which are consistent with the results by Morand et al. [8].

Take the optimized standard GTO launched by Ariane 5 in Eq. (55) as an example. According to the desired initial orbital geometry for the long-period perturbation, we have  $\omega_0 = 178^\circ$  and  $\Omega_0 = 195^\circ$ . As for the short-period perturbation, we set the initial solar argument of latitude to be  $100^\circ$  or  $280^\circ$ , and then the initial azimuth of  $\mathbf{d}_S$  is about  $90^\circ$  or  $270^\circ$ . Then, the short-period eccentricity oscillation is initially at the beginning of an increase phase.

## 6. Verification of lifetime reduction

### 6.1. Verification using simple dynamical models

We first verify the desired initial orbital geometry using a numerical simulation performed on the doubly-averaged orbital model DAOD and the triply-averaged orbital model TAOD without atmospheric drag. TAOD contains only the long-period oscillation, while DAOD contains both the long-period oscillation and the 180-day short-period oscillation induced by the solar orbital motion. The simulation is with the optimized standard GTO launched by Ariane 5 in Eq. (55) with  $\Omega_0 = 195^\circ$  and the initial solar argument of latitude equal to  $100^\circ$ , which is the desired initial orbital

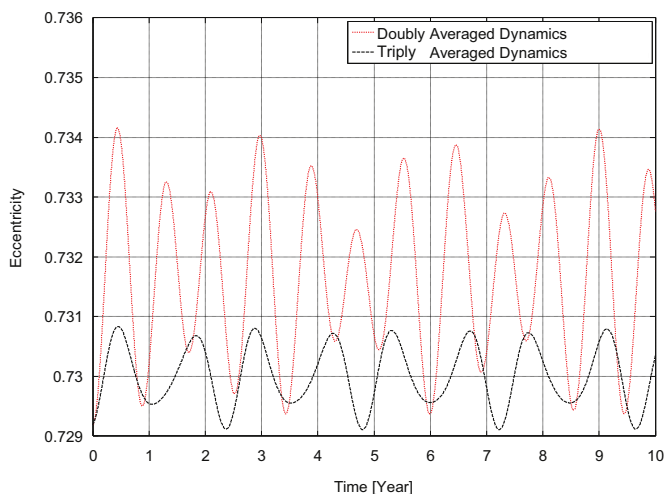


Fig. 12. Time history of  $e$  of a standard GTO launched by Ariane 5 with  $\Omega_0 = 195^\circ$  without drag.

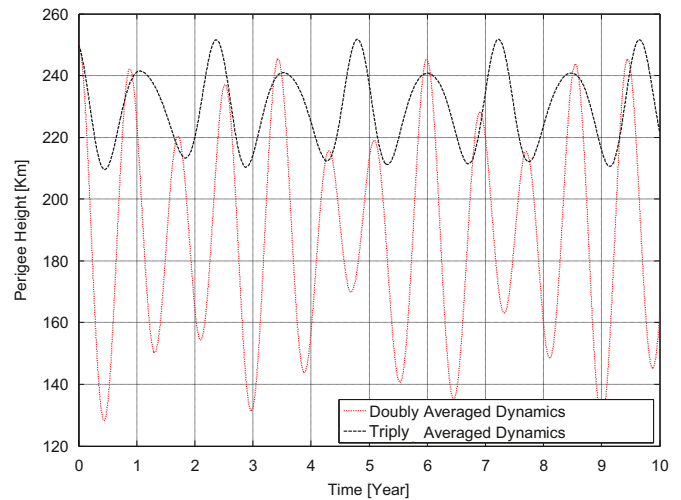


Fig. 13. Time history of  $h_p$  of a standard GTO launched by Ariane 5 with  $\Omega_0 = 195^\circ$  without drag.

geometry obtained in Section 5. The time histories of  $e$  and  $h_p$  are given in Figs. 12 and 13, respectively.

According to Figs. 12 and 13, we can see that both the long- and short-period oscillations of the perigee height are initially at the beginning of a decrease phase. Consequently, the long-period perigee is oscillating nearly always below the initial perigee, and the short-period perigee has the long-period perigee as its upper envelope. The resulting superposition of the oscillations in DAOD is always below the initial perigee and the maximum distance from the initial perigee is as large as 120 km. By using the luni-solar perturbations, the perigee height can be lowered from 250 km to 130 km, where the dense atmosphere can decay the orbit fast. Thus, the desired initial orbital geometry has been verified.

### 6.2. Verification using full dynamical models

We also verify the desired initial orbital geometry using the full orbital dynamical models, including the orbital models SAOD, DAOD, and TAOD derived in this work, as well as HPOP and LOP. The simulation will be performed for the optimized standard GTO given in Eq. (55) with the desired initial orbital geometry given in

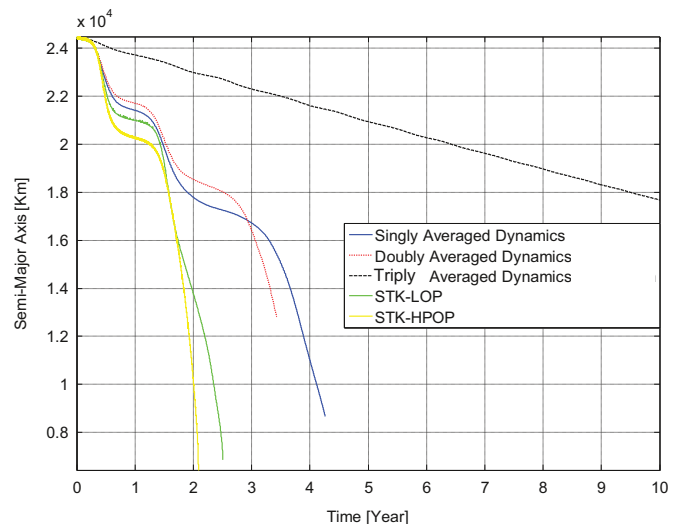
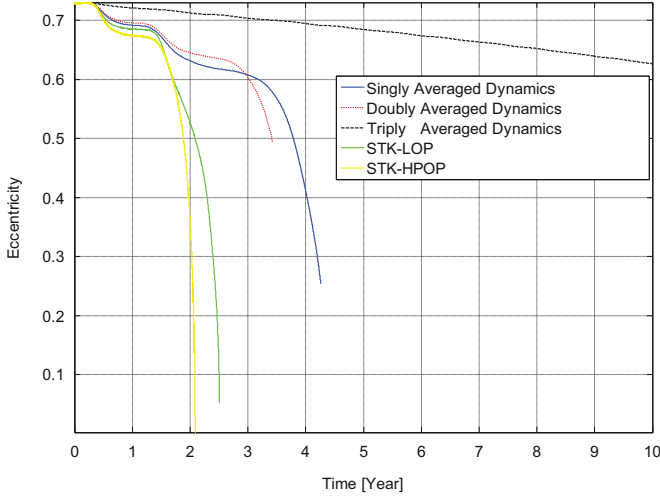
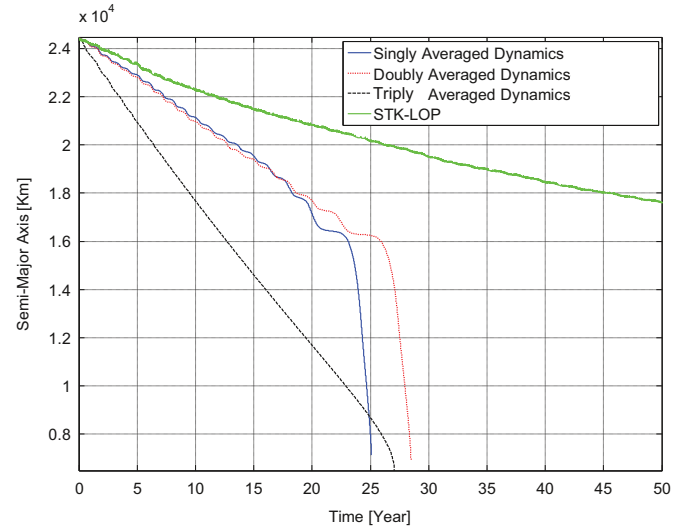


Fig. 14. Time history of  $a$  of a standard GTO with the desired initial orbital geometry.





**Fig. 15.** Time history of  $e$  of a standard GTO with the desired initial orbital geometry.



**Fig. 17.** Time history of  $a$  of a standard GTO with another initial orbital geometry.

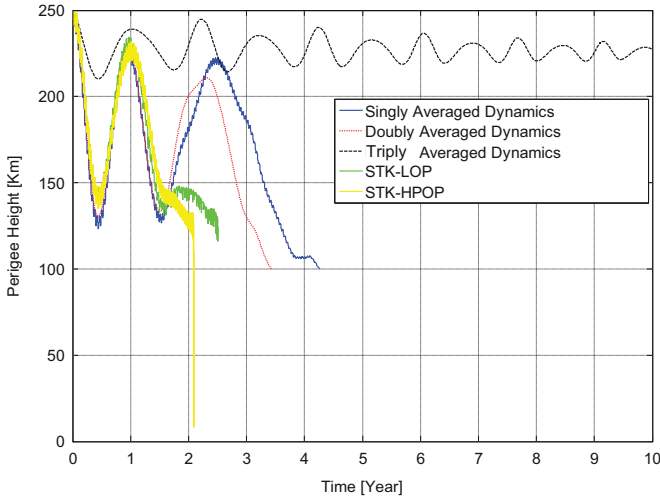


**Fig. 16.** Time history of  $h_p$  of a standard GTO with the desired initial orbital geometry.

### Section 5.3.2,

$$i_0 = 6^\circ, \quad h_{a0} = 35,943 \text{ km}, \quad h_{p0} = 250 \text{ km}, \quad \omega_0 = 178^\circ, \\ \Omega_0 = 195^\circ. \quad (68)$$

The initial solar argument of latitude is equal to  $100^\circ$  and  $\text{AMR} = 0.01 \text{ m}^2/\text{kg}$ . The epoch is set to be 2 July 2015 12:00:00 UTC according to the initial solar argument of latitude. Other system parameters are all the same as the simulation in Section 4. Time histories of  $a$ ,  $e$ , and  $h_p$  propagated by all the orbital models are given in Figs. 14–16, respectively.

From Figs. 14–16 we can see that the desired initial orbital geometry obtained by us has been verified in the full orbital models: in all the orbital models the initial perigee height is lowered by the luni-solar perturbations significantly through both the long- and short-period oscillations. The perigee is always below the initial perigee, and can be as low as 125 km. Consequently, the orbit is decaying fast. The orbital lifetimes predicted by HPOP, LOP, DAOD, and SAOD are only 2 years, 2.5 years, 3.4 years, and 4.3 years, respectively. Notice that since TAOD eliminates the short-period oscillation induced by the solar orbital motion, which significantly lowers the perigee height, it cannot capture the system evolution accurately. The differences between the orbits of

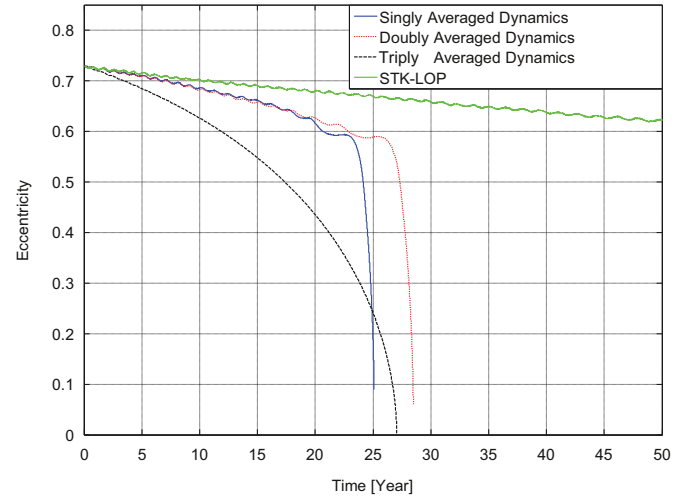


**Fig. 18.** Time history of  $e$  of a standard GTO with another initial orbital geometry.

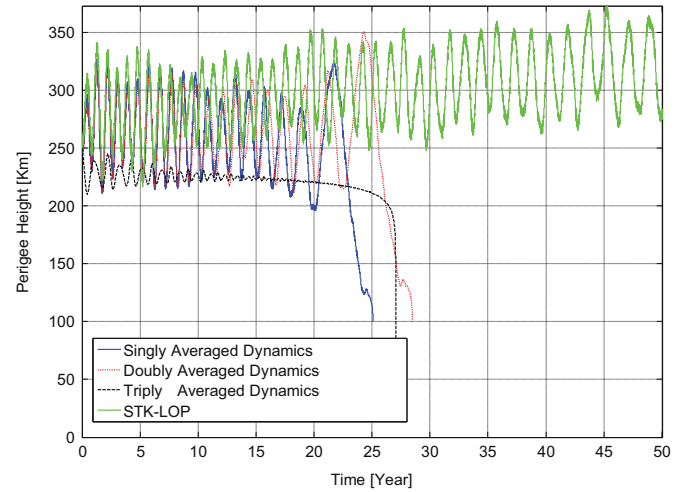


**Fig. 19.** Time history of  $h_p$  of a standard GTO with another initial orbital geometry.

HPOP, LOP, DAOD, and SAOD after 1.5 years can be attributed to the different atmospheric density models and the 14-day short-period oscillation induced by the lunar orbital motion, which is eliminated in DAOD.

To show the advantage of the desired initial orbital geometry better, we give another simulation with the same initial conditions and system parameters except a different initial solar argument of latitude that is equal to  $10^\circ$ . The epoch time is set to be 2 April 2015 6:00:00 UTC accordingly. This simulation will not be carried out with HPOP, since the orbital lifetime is long and it is very time consuming. Time histories of  $a$ ,  $e$ , and  $h_p$  propagated by the orbital models are given in Figs. 17–19, respectively.

We can see that, with the initial solar argument of latitude equal to  $10^\circ$ , although the long-period perturbation still lowers the initial perigee height, the short-period solar perturbation raises the initial perigee height. Consequently, compared with our desired initial orbital geometry, the orbital lifetime has been enhanced significantly to more than 25 years, even to more than 50 years as predicted by LOP.

## 7. Conclusions

Numerical simulations show that the singly-averaged GTO model derived in the present paper can capture the main effects of the dominant perturbations quite well, and can provide computationally efficient orbit propagation in a time span of several years. The orbital model, which is formulated in a vectorial form, gives the explicit relation between the orbit variation and the underlying physics.

The long- and short-period luni-solar perturbation effects have been isolated and studied separately. We have shown that the long-period perturbation is induced by the precession of the GTO orbital plane and apsidal line, whereas the short-period perturbation is induced by the periodic luni-solar orbital motions. We have found that the magnitudes of the long- and short-period solar perturbation depend on the declinations of the solar orbital momentum and solar position with respect to the GTO orbital plane, respectively; the phases of the long- and short-period solar perturbation depend on the azimuths of the solar orbital momentum and solar position with respect to the GTO apsidal line, respectively. The desired initial orbital geometry, which is found based on the distribution of the luni-solar perturbations with respect to the orbital geometry, can provide an orbital lifetime that is reduced by the luni-solar perturbations to the maximum extent in the statistical sense.

## Acknowledgements

This work was supported by the European Research Council Starting Independent Researcher Grant - 278231: Flight Algorithms for Disaggregated Space Architectures (FADER).

## References

- [1] H. Klinkrad, *ESA Space Debris Mitigation Handbook*, European Space Agency, Darmstadt, Germany, 2003.
- [2] D. King-Hele, Lifetime prediction for satellites in low-inclination transfer

- orbits, *J. Br. Interplanet. Soc.* 35 (1982) 339–344.
- [3] G. Janin, Decay of debris in geostationary transfer orbit, *Adv. Space Res.* 11 (6) (1991) 161–166, [http://dx.doi.org/10.1016/0273-1177\(91\)90247-H](http://dx.doi.org/10.1016/0273-1177(91)90247-H).
- [4] K. Siebold, R. Reynolds, Lifetime reduction of a geosynchronous transfer orbit with the help of lunar-solar perturbations, *Adv. Space Res.* 16 (11) (1995) 155–161, [http://dx.doi.org/10.1016/0273-1177\(95\)98767-I](http://dx.doi.org/10.1016/0273-1177(95)98767-I).
- [5] A. Takano, T. Tajima, Y. Kanoh, Recent efforts toward the minimization of GTO objects and its practices in NASDA, *Acta Astronaut.* 40 (11) (1997) 807–813, [http://dx.doi.org/10.1016/S0094-5765\(97\)00129-X](http://dx.doi.org/10.1016/S0094-5765(97)00129-X).
- [6] R. Sharma, P. Bandyopadhyay, V. Adimurthy, Consideration of lifetime limitation for spent stages in GTO, *Adv. Space Res.* 34 (5) (2004) 1227–1232, <http://dx.doi.org/10.1016/j.asr.2003.10.044>.
- [7] B.C. Da Costa, M. Bernardini, M. Cerf, M. Fessard, S. Reynaud, Long-term semi-analytical orbit propagation tool for future European launchers design, in: *AIAA/AAS Astrodynamics Specialist Conference*, no. AIAA 2012–4743, Minneapolis, Minnesota, 13–16 August, 2012.
- [8] V. Morand, C. Le Fèvre, A. Lamy, H. Fraysse, F. Deleflie, Dynamical properties of geostationary transfer orbits over long time scales: consequences for mission analysis and lifetime estimation, in: *AIAA/AAS Astrodynamics Specialist Conference*, no. AIAA 2012–4968, Minneapolis, Minnesota, 13–16 August, 2012.
- [9] A. Lamy, C. Le Fèvre, B. Sarli, Analysis of geostationary transfer orbit long term evolution and lifetime, *J. Aerosp. Eng. Sci. Appl.* 4 (3) (2012) 12–27, <http://dx.doi.org/10.7446/jaesa.0403.02>.
- [10] F. Bonaventure, S. Locoche, A.-H. Gicquel, De-orbitation studies and operations for SPIRALE GTO satellites, in: *23rd International Symposium on Space Flight Dynamics*, Pasadena, California, 29 October–2 November, 2012.
- [11] E. David, V. Braun, Re-entry analysis comparison with different solar activity models of spent upper stage using ESA's DRAMA tool, in: *The 6th IAASS Conference*, Montreal, Canada, 21–23 May, 2013.
- [12] E. Upton, A. Bailie, P. Musen, Lunar and solar perturbations on satellite orbits, *Science* 130 (3390) (1959) 1710–1711, <http://dx.doi.org/10.1126/science.130.3390.1710>.
- [13] B.E. Shute, Prelaunch Analysis of High Eccentricity Orbits, Technical Reports NASA Technical Note, NASA TN D-2530, NASA Goddard Space Flight Center, 1964.
- [14] S. Paddock, B. Shote, IMP-C Orbit and Launch Time Analysis, Technical Report Doc. No. X-643–65–40, NASA Goddard Space Flight Center, 1965.
- [15] B.E. Shute, J. Chiville, Lifetimes of Highly Eccentric Satellites, Technical Report Doc. No. X-643–65–402, NASA Goddard Space Flight Center (1965).
- [16] B.E. Shute, J. Chiville, The lunar-solar effect on the orbital lifetimes of artificial satellites with highly eccentric orbits, *Planet. Space Sci.* 14 (4) (1966) 361–369, [http://dx.doi.org/10.1016/0032-0633\(66\)90073-0](http://dx.doi.org/10.1016/0032-0633(66)90073-0).
- [17] G. Cook, D.W. Scott, Lifetimes of satellites in large-eccentricity orbits, *Planet. Space Sci.* 15 (10) (1967) 1549–1556, [http://dx.doi.org/10.1016/0032-0633\(67\)90088-8](http://dx.doi.org/10.1016/0032-0633(67)90088-8).
- [18] G. Janin, E. Roth, Decay of a highly eccentric satellite, *Celest. Mech.* 14 (1) (1976) 141–149, <http://dx.doi.org/10.1007/BF01247141>.
- [19] J.D. Fischer, The evolution of highly eccentric orbits (Master's thesis), Department of Aeronautics and Astronautics, Massachusetts Institute of Technology, 1998.
- [20] Y. Kozai, Secular perturbations of asteroids with high inclination and eccentricity, *Astron. J.* 67 (9) (1962) 591–598, <http://dx.doi.org/10.1086/108790>.
- [21] C. Le Fèvre, H. Fraysse, V. Morand, A. Lamy, C. Cazaux, P. Mercier, C. Dental, F. Deleflie, D. Handschuh, Compliance of disposal orbits with the French Space Operations Act: the Good Practices and the STELA tool, *Acta Astronaut.* 94 (1) (2014) 234–245, <http://dx.doi.org/10.1016/j.actaastro.2013.07.038>.
- [22] M. Milankovitch, *Kanon der Erdbestrahlung und seine Anwendung auf das Eiszeitenproblem*, Canon of Insolation and the Ice-age Problem, Königlich Serbische Akademie (English translation by Israel Program for Scientific Translations), Belgrade, 1941.
- [23] A.J. Rosengren, D.J. Scheeres, Long-term dynamics of high area-to-mass ratio objects in high-Earth orbit, *Adv. Space Res.* 52 (8) (2013) 1545–1560, <http://dx.doi.org/10.1016/j.asr.2013.07.033>.
- [24] A.J. Rosengren, D.J. Scheeres, On the Milankovitch orbital elements for perturbed Keplerian motion, *Celest. Mech. Dyn. Astron.* 118 (3) (2014) 197–220, <http://dx.doi.org/10.1007/s10569-013-9530-7>.
- [25] A. Roy, P. Moran, Studies in the application of recurrence relations to special perturbation methods: III. Non-singular differential equations for special perturbations, *Celest. Mech.* 7 (2) (1973) 236–255, <http://dx.doi.org/10.1007/BF01229950>.
- [26] D.G. King-Hele, *Theory of Satellite Orbits in an Atmosphere*, Butterworths, London, 1964.